Electron Microprobe Analysis

Course 12.141

Notes

Dr. Nilanjan Chatterjee

The electron microprobe provides a complete micron-scale quantitative chemical analysis of inorganic solids. The method is nondestructive and utilizes characteristic x-rays excited by an electron beam incident on a flat surface of the sample. This course provides an introduction to the theory of x-ray microanalysis by wavelength and energy dispersive spectrometry (WDS and EDS), ZAF matrix correction procedures, and scanning electron imaging techniques using backscattered electron (BE), secondary electron (SE), x-ray (elemental mapping), and cathodoluminescence (CL) signals. Lab sessions involve hands-on use of the JEOL JXA-8200 Superprobe.

MIT Electron Microprobe Facility

Massachusetts Institute of Technology
Department of Earth, Atmospheric & Planetary Sciences
Room: 54-1221, Cambridge, MA 02139
Phone: (617) 253-1995; Fax: (617) 253-7102
e-mail: e-probe-www@mit.edu
web: http://web.mit.edu/e-probe/www/

TABLE OF CONTENTS

1. INTRODUCTION

The electron microprobe, also known as the electron probe micro-analyzer (EPMA), uses x-ray spectrometry to identify and measure concentration of elements in microscopic volumes of the specimen. In EPMA, a finely focused electron beam interacts with the sample to generate backscattered electrons (BSE), secondary electrons (SE), characteristic x-rays and light known as cathodoluminescence (CL). By scanning the electron beam over a surface of the sample, these signals can be used to obtain high resolution scanning electron images, x-ray maps showing spatial distribution of elements, and CL images for phase (element and compound) identification, estimation of phase distribution and proportions, trace element compositional variation and surface textural analysis of multi-phase composites. Characteristic x-rays generated from a microscopic volume in spot mode operation (i.e., beam not scanning) are utilized to obtain a complete quantitative chemical analysis. Sample preparation is minimal, but a well-polished surface is required for accurate quantitative analysis. Although the EPMA is mostly used in the characterization of inorganic materials, organic compounds such as polymers and biological specimens can also be examined by following special procedures and sample preparation techniques.
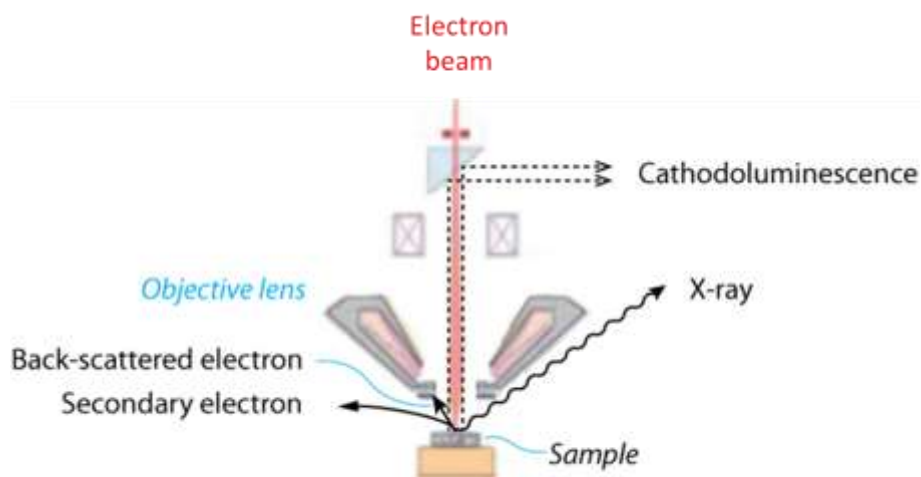
In the JEOL JXA-8200 Superprobe, the electron beam is generated from a heated tungsten filament by thermionic emission in a potential difference typically between 5 and 30 kV. There is also an option to use a LaB_6 single crystal as a thermionic emission source that provides a highly stable, high intensity and smaller diameter electron beam for higher resolution imaging and more reliable chemical analysis. The beam is focused by two sets of coils, the condenser and the objective lenses, and several apertures that produces a final beam diameter between 1 nm and 1 μm. Beam currents range between 1 pA and 1 μA. A reflected light optical microscope is mounted co-axially with the electron beam for accurately setting the working distance between the sample and the objective lens. Both energy dispersive and wavelength dispersive spectrometers (EDS and WDS) are available for qualitative and quantitative analysis. The beam can be rastered over the sample to produce images in the magnification range of 40-360,000 times. X-ray elemental maps are obtained by using the emitted x-rays as the signal source instead of BSE or SE. CL analysis is performed with the xClent system to acquire high resolution color images and to identify

and quantify impurities and dopants in natural and synthetic semiconductors. A high vacuum, typically in the pressure range of 2×10^{-5}-10^{-6} torr (about one-billionth of the atmospheric pressure), is maintained in the column and sample chamber by a combination of mechanical and diffusion pumps.
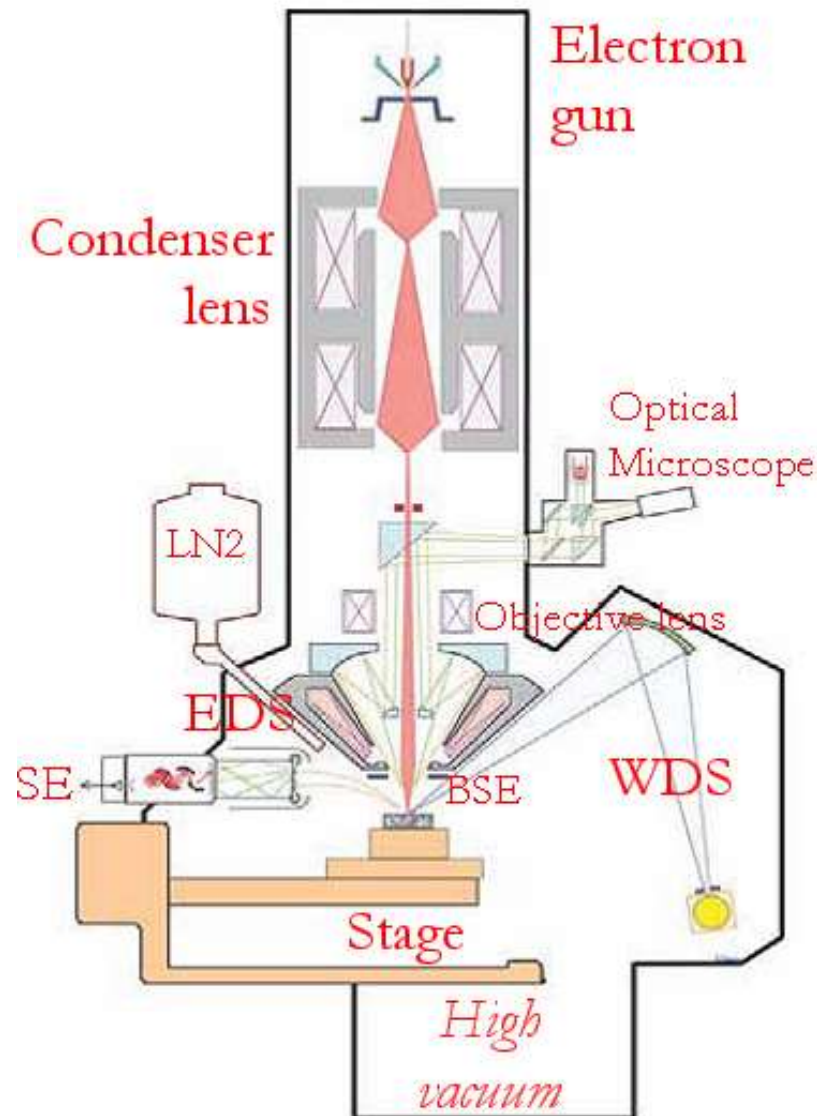
2. ELECTRON SPECIMEN INTERACTIONS

When an electron beam interacts with a target (i.e., the sample), the electrons are scattered by the target atoms. There are two types of electron scattering:

Elastic scattering	Inelastic scattering
$E_1 = E_0$, large ϕ_e	$E_1 < E_0$, small ϕ_i

$(\phi_e >> \phi_i)$
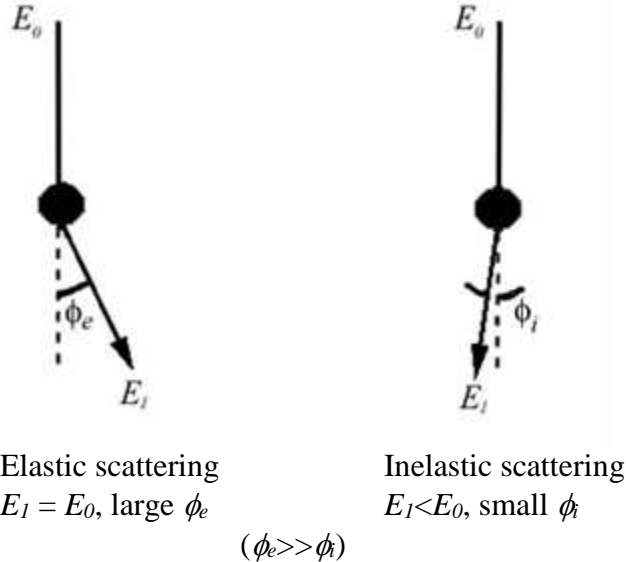
where, E_0 is the energy of the incident electron; E_1, the energy of the electron after scattering; ϕ_e, the elastic scattering angle; and ϕ_i, the inelastic scattering angle.

2.1. ELASTIC SCATTERING

Elastic scattering affects the trajectories of the beam electrons without significantly altering their kinetic energy. Back-scattered electrons are elastically scattered beam electrons. The scattering probability or **cross-section** of elastic scattering, Q, for scattering angles greater than ϕ_e, is given by the screened Rutherford expression:

$$Q_{(>\phi_e)} = 1.62 \times 10^{-20} \left(\frac{Z^2}{E^2}\right) \cot^2\left(\frac{\phi_e}{2}\right) \tag{2.1}$$

events.cm^2/e$^-$.atom; where, Z is the atomic number; and E, the incident electron energy (keV). Q is thus proportional to the square of Z of the target, and inversely proportional to the square of E of the electron beam.

### 2.1.1. Electron backscattering

When the elastic scattering angle is greater than 90°, backscattering occurs. It may also occur through multiple scattering at high angles. The **electron backscatter coefficient**, η, is the fraction of beam electrons scattered backward:

$$\eta = \frac{n_{BSE}}{n_B} = \frac{i_{BSE}}{i_B} \tag{2.2}$$

where, n_B is the number of incident beam electrons and n_{BSE} is the number of back-scattered electrons (i's denote current). For compounds, η is given as:

$$\eta = \sum_j C_j \eta_j \tag{2.3}$$

where, j denotes the constituent elements and C_j the concentration j in the compound. η increases monotonically with atomic number and it is independent of beam energies above 5 keV.
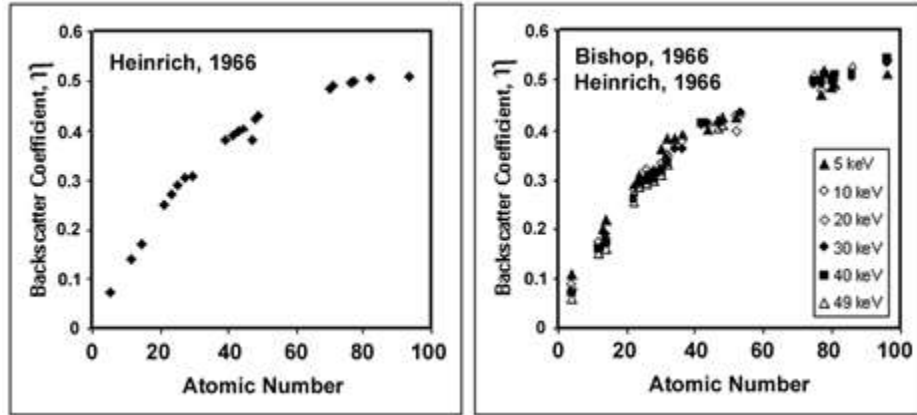
2.1.2. Electron interaction volume

The electron range is the distance between the point where the beam electron enters the specimen and the point where it loses all its energy and exits the specimen as sample current. The **Kanaya-Okayama range** takes into the account the combined effects of elastic and inelastic scattering and is given by:

$$R_{KO} = K \frac{E_0{}^n}{\rho} \tag{2.4}$$

(μm), where, $K = 0.0276 \frac{A}{Z^{0.889}}$, A (g/mole), the atomic weight, Z, the atomic number, ρ (g/cm^3), the density, E_0 (keV), the incident beam energy, and $n = 1.67$. Typical ranges (at perpendicular beam incidence and 15 keV beam energy) are 1.8 μm for C, 1.1 μm for Fe and 0.8 μm for U.
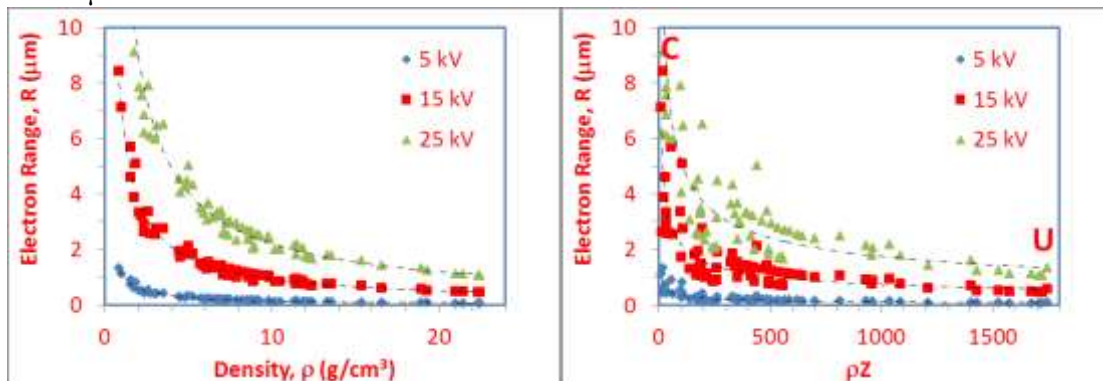
Monte Carlo electron-trajectory simulations show that the size of the electron interaction volume increases with the incident beam energy. There is less elastic scattering at higher beam energies (Eqn. 2.1) and the electrons are able to penetrate deeper. The interaction volume decreases with increasing atomic number as predicted by Eqn. 2.1. Experiments suggest that the interaction volume is pear-shaped for low atomic number targets and spherical for higher atomic number targets. Most of the backscattered electrons come from the top part of the interaction volume, e.g., 90% are generated in the top 17% in Au and the top 29% in C (for perpendicular beam incidence and 20 keV beam energy).

2.2. INELASTIC SCATTERING

Inelastic scattering involves transfer of energy from the beam electrons to the specimen atoms, and concomitant generation of secondary electrons, Auger electrons, characteristic x-rays, bremsstrahlung (continuum) x-rays, and light (cathodoluminescence). The trajectory of the beam electron is not altered significantly.

2.2.1. Secondary electron generation

Some sample electrons mobilized through inelastic scattering by beam electrons overcome the surface energy barrier and escape from the sample. These electrons are known as *secondary electrons*. They have lower energies (<50 eV; majority <10 eV) compared to back-scattered electrons.

The *secondary electron coefficient*, δ, is defined as

$$\delta = \frac{n_{SE}}{n_B} = \frac{i_{SE}}{i_B} \tag{2.5}$$

where, n_B is the number of incident beam electrons and n_{SE} is the number of secondary electrons (*i*'s denote current). Compared to the backscatter coefficient, δ is relatively insensitive to the target atomic number. It generally increases with a decrease in the beam energy.

Although sample electrons are mobilized throughout the interaction volume, their escape probability from the surface of the sample decreases sharply with depth. The *escape depth of secondary electrons is only about 1/100 of that for backscattered electrons* for incident beam energies in the range 10-30 keV. Hence, secondary electrons are useful in studying the surface characteristics of the sample. Samples are commonly coated with a thin film of gold that enhances the secondary electron yield.

2.2.2. Characteristic x-ray generation: inner-shell ionization

X-rays are electromagnetic radiations in the energy range of about 0.12 to 120 keV (wavelength range: of 10 to 10^{-2} nanometer). The typical range of x-ray energies analyzed in the EPMA are between 0.12 and 10 keV. An element is identified by its characteristic set of emitted x-ray energies.
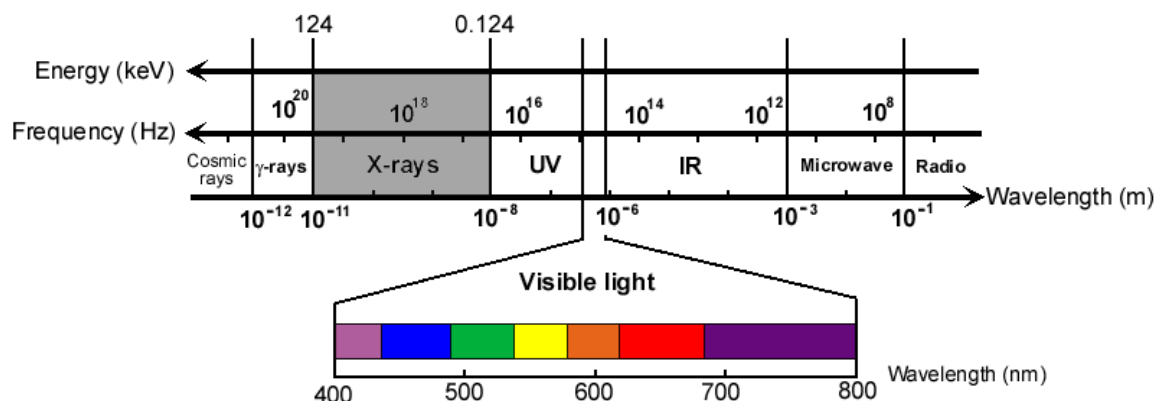
The *energy, E,* of an x-ray is given by

$$E = h\nu \tag{2.6}$$

Where, h is the Planck's constant (6.626×10^{-34} Joule.sec = 6.626×10^{-34} / 1.6021×10^{-16} keV.sec) and the frequency $\nu = c/\lambda$, c being the speed of light in vacuum (2.99793×10^{17} nm/sec) and λ being the **wavelength.** Thus, the wavelength is related to the energy as:

$$\lambda = h\frac{c}{E} = 1.2398\frac{1}{E} \tag{2.7}$$

where, λ is in nm and E is in keV.

When the beam electrons are scattered inelastically, tightly bound inner shell electrons from the target atoms may be ejected if the beam energy is higher than the **critical excitation energy,** E_C (also known as **ionization energy** or **absorption edge energy**), of the target atomic shell. The **overvoltage,** U, of the electron beam is expressed as:

$$U = \frac{E}{E_c} \tag{2.8}$$
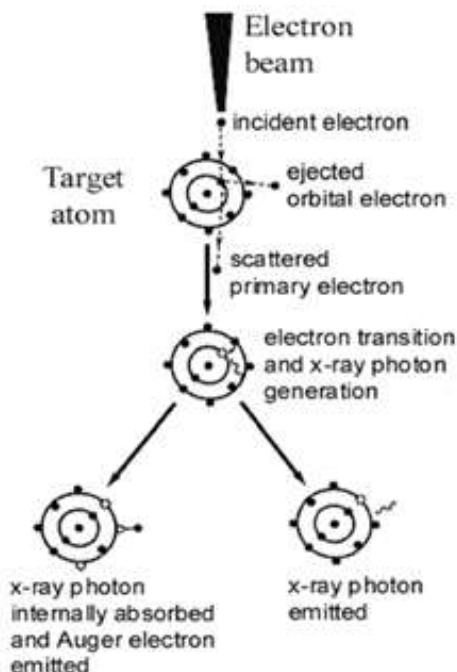
where, E is the beam energy. U must be greater than unity for ionization to occur. The energy of the beam electron is diminished by an amount equal to E_C. Subsequently, relaxation of the target atom from its excited state that involves transfer of an outer shell electron to the ionized inner shell, results in the generation of a characteristic x-ray. This x-ray may be emitted from the atom, or it may be internally absorbed while ejecting another outer shell electron (an Auger electron). The fraction of x-rays emitted (**characteristic x-ray yield** or **fluorescent yield,** ω) for a specific shell increases with the atomic number, whereas the **Auger yield,** α, decreases.
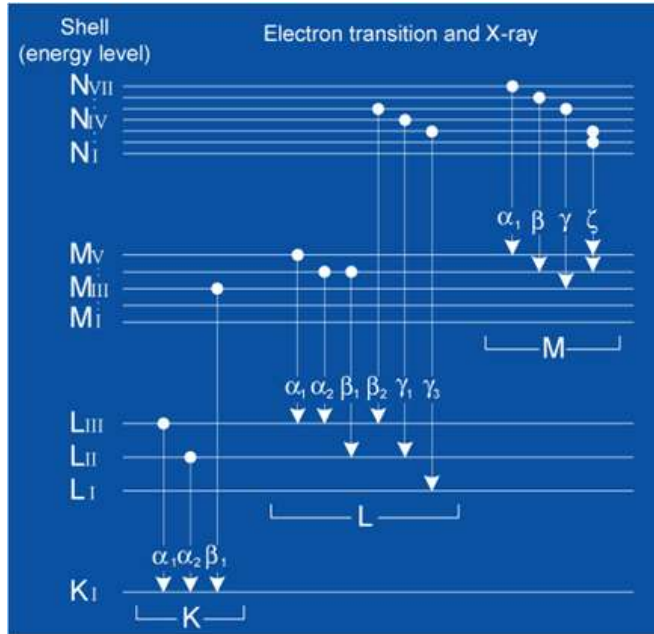
Characteristic x-rays are named according the electron transition between shells as follows:

Kα: from L-shell to K-shell,
Kβ: from M-shell to K-shell,
Lα: from M-shell to L-shell,
Mα: from N-shell to M-shell,
etc.

The **cross-section of inner shell ionization** is given by Bethe as follows:

$$Q = 6.51 \times 10^{-20} \left(\frac{n_S b_S}{U E_c^2} \right) \ln(c_S U) \tag{2.9}$$

ionizations.cm^2/e$^-$.atom), where n_S is the number of electrons in a shell or subshell (e.g., n_S=2 for a K shell), b_S and c_S are constants for a particular shell, E_c (keV) is the critical excitation energy of the shell, and U is the overvoltage. For the K-shell, the constants are b_S=0.3 and c_S=1 at U<4, and b_S=0.9 and c_S=0.65 at 4<U<25.

Energy lost by the beam electrons due to inelastic scatterings is given by Bethe as:

$$\frac{dE}{ds} = -7.85 \times 10^{-4} \left(\frac{Z\rho}{A E_m} \right) ln \left(1.166 \frac{E_m}{J} \right) \tag{2.10}$$

where, the constant is equal to $2\pi e^4 N_0$; e being the electronic charge and N_0, the Avogadro's number; Z is the atomic number; A (g/mole), the atomic weight, ρ (g/cm^3), the density, E_m (keV), the average energy along path segment s, and J (keV), the mean ionization potential given by Berger & Seltzer:

$$J = (9.76Z + 58.82\ Z^{-0.19}) \times 10^{-3} \tag{2.11}$$

The **electron stopping power** of a material, S, is a function of its density and rate of energy loss of the beam electrons (Eqn. 2.10). It is defined by the following expression:

$$S = -\frac{1}{\rho} \frac{dE}{ds} \tag{2.12}$$

where, ρ is the density and $\frac{dE}{ds}$, the rate of electron energy loss with distance.

The cross-section of inner-shell ionization is maximum at overvoltage values between 3 and 7. The cross-section of all types of inelastic scattering decreases with increasing incident beam energy.
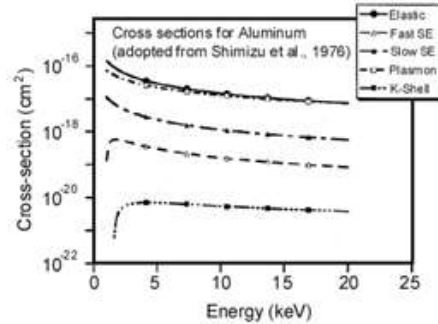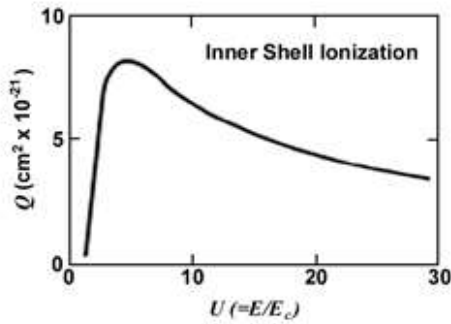
2.2.3. X-ray production volume

Since characteristic x-rays are produced only when the incident beam energy exceeds E_C, the x-ray range is always smaller than the electron range. The **x-ray range** according to Castaing is:

$$R = 0.033(E_0^{1.7} - E_c^{1.7})\frac{A}{\rho Z} \tag{2.13}$$

(μm). The range of primary x-ray generation is critical in estimating the sampling volume in x-ray microanalysis.
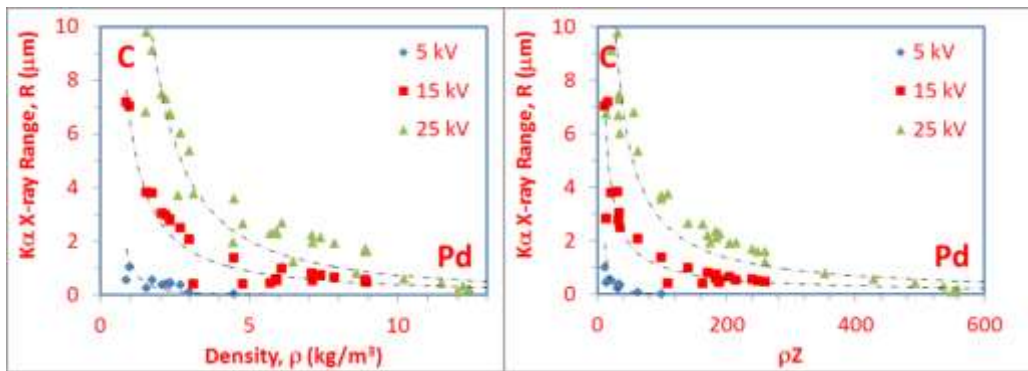
The x-ray range is always smaller than the electron range. However, it is larger than the range for backscattered and secondary electrons. On the other hand, the range for secondary x-ray fluorescence (see section 3.1.3) is much larger.
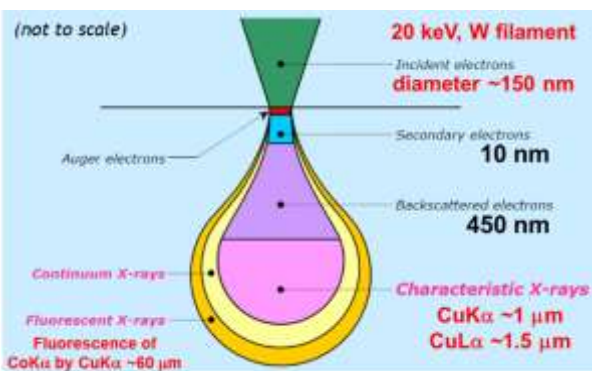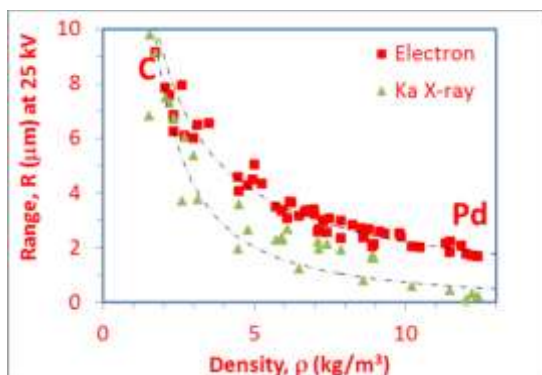
The distribution of x-ray generation sites within the interaction volume is given by the **depth-distribution function**, $\phi(\rho z)$, which shows the number of x-rays generated in each layer of thickness dz with depth in the specimen, normalized to the number of x-rays generated in a freestanding layer of the same material with thickness dz.

$$I_{generated} = \phi(\Delta\rho z) \int_0^\infty \phi(\rho z) d(\rho z) \qquad (2.14)$$

where, $\phi(\Delta\rho z)$ is the intensity generated in a freestanding layer of thickness $\Delta\rho z$. The upper layers produce more x-rays than a freestanding layer because the electrons are free to travel randomly between layers by multiple scattering events.

$\phi(\rho z)$, as a histogram with specimen layers of thickness dz as bins. The intensity in each layer is normalized by intensity generated in a freestanding layer under the same conditions.
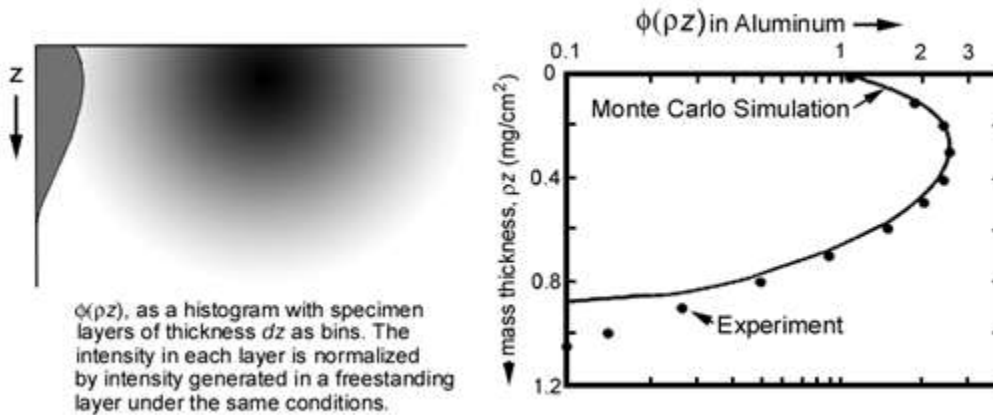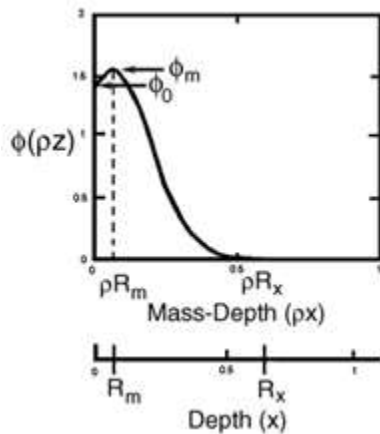
With increasing depth, however, the electrons lose their energy and finally, their ability to ionize inner-shells as the instantaneous overvoltage drops below unity.

The value of $\phi(\rho z)$ at the surface, ϕ_0; the maximum value of $\phi(\rho z)$, ϕ_m; the depth at ϕ_m, R_m; and the maximum depth where $\phi(\rho z)$ is zero, R_x, are parameters used to describe a $\phi(\rho z)$ distribution. Both R_m and R_x decrease with atomic number (Z) and increase with beam energy (E_0). ϕ_0 increases with E_0.

2.2.4. Bremsstrahlung or continuum x-ray generation

As the beam electrons approach the target atoms, some of the electrons lose a part or all of their energy by deceleration in the Coulombic field created by the outer shell electrons of the target atom. The energy lost by the beam electron is converted into bremsstrahlung or continuum x-rays with maximum energies up to the total initial energy of the beam electron. The maximum continuum x-ray energy, known as the Duane-Hunt limit, provides a means for accurately measuring the energy of the electron beam.
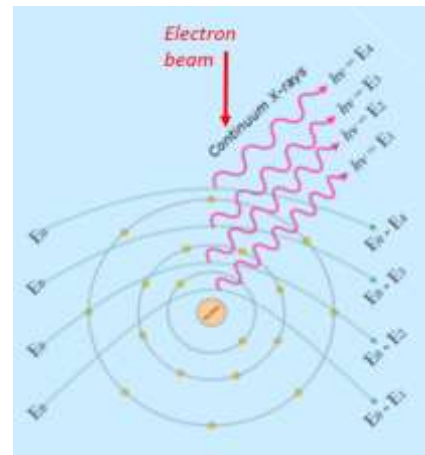
2.2.5. Cathodoluminescence

When semiconductors interact with energetic electrons, they produce long-wavelength ultraviolet, visible and infrared radiations known as cathodoluminescence (CL). Cathodoluminescent materials have a filled valence band and an empty conduction band separated by an energy gap, E_{gap}. When an energetic beam electron scatters inelastically, an electron from the valence band moves to the conduction band leaving a hole in the valence band. The electron and the hole eventually recombine to release light energy equal to E_{gap}., characteristic of the semiconductor. However, presence of impurity creates additional energy states outside the conduction band, and the resulting light may have different energy. Thus, cathodoluminescence spectrometry can be used characterize impurity.
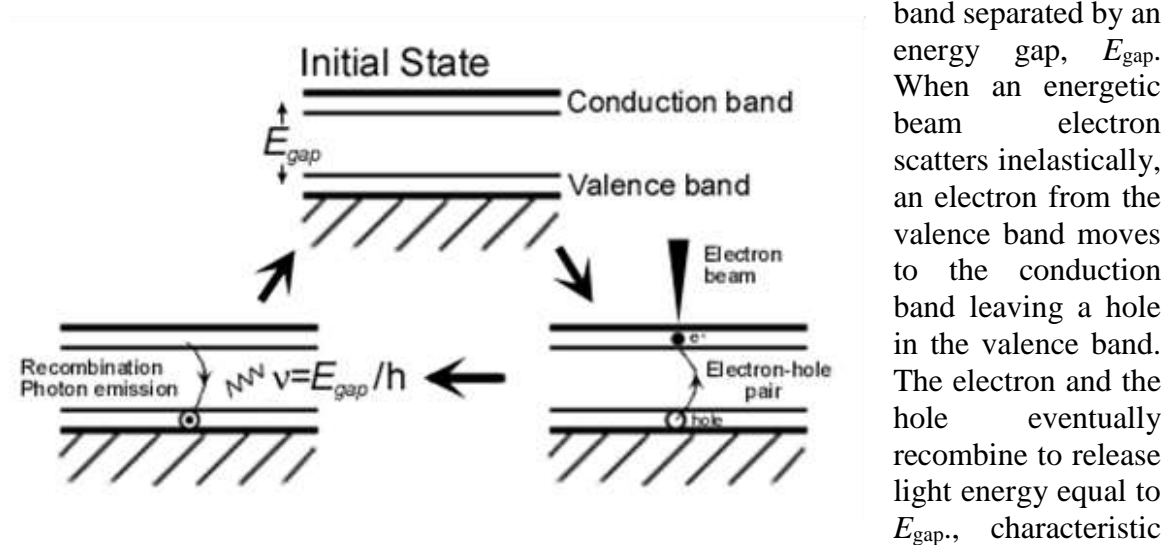
The cathodoluminescence production volume strongly depends on the electron beam energy. However, most of the light is generated from a region close to the beam impact point.
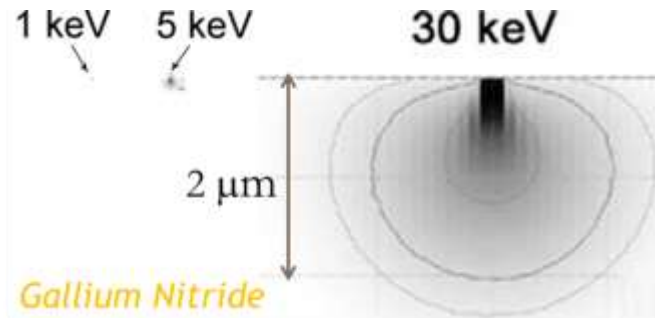
3. QUANTITATIVE X-RAY SPECTROMETRY

The *primary generated* characteristic x-ray intensities are roughly proportional to the respective mass-fractions of the emitting elements.

$$C_i \propto I_i \tag{3.1}$$

where, C_i and I_i are the weight concentration and primary generated x-ray intensity of element *i*. In quantitative analysis, the intensity is compared against the intensity of the same element generated from a standard, $I_{(i)}$, with a known concentration $C_{(i)}$ of that element. The ratio of the intensity from the sample and standard is known as the ***k-ratio***.

$$\frac{C_i}{C_{(i)}} \propto \frac{I_i}{I_{(i)}} \tag{3.2}$$

where,

$$\frac{I_i}{I_{(i)}} = k_i \tag{3.3}$$

Because of interaction of the primary generated x-rays with the specimen atoms, the emitted x-rays have a different intensity from the generated intensity. This matrix effect is taken into account by modifying the above equation as:

$$\frac{C_i}{C_{(i)}} = k_i \cdot [ZAF]_i \tag{3.4}$$

where, $[\mathbf{ZAF}]_i$ is the ***matrix correction factor*** for element *i*. However, the matrix correction depends on the composition of the specimen. Since the composition is unknown before the analysis, the ZAF factors are also unknown. Therefore, the concentration C_i is determined through iteration. The measured k-ratios (k_i) are used as a first estimate of the concentrations and the ZAF factors are calculated. The concentrations (C_i) are then calculated by multiplying the k-ratios with the corresponding ZAF factors calculated in the last step. A new set of ZAF factors are then calculated using the C_i values obtained in the last step, and concentrations are recalculated by multiplying the ZAF's with the original k-ratios. The process is repeated until the calculated C_i does not change from the previous step. The following flow-chart demonstrates the procedure:
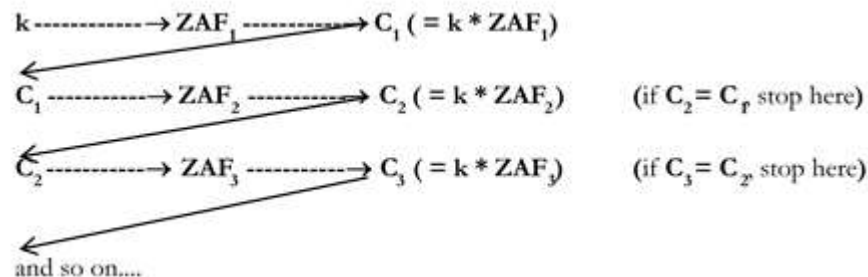
3.1. MATRIX CORRECTIONS

The atomic number correction, **Z**, the absorption correction, **A**, and the fluorescence correction, **F** are the three constituents of the matrix correction.

3.1.1. Atomic number correction (**Z**)

The atomic number correction depends on the average atomic numbers of the specimen and the standard. It is a function of the electron back-scattering factor (R) and the electron stopping power (S, Eqn. 2.12). R is the ratio of number of x-rays actually generated to number of x-rays generated if there were no backscatter.

According to Duncumb & Reed (1968), the atomic number correction $\mathbf{Z}_i$ for element i is:

$$\mathbf{Z}_i = \frac{R_i \int_{E_c}^{E_0} \frac{Q}{S} dE}{R_i^* \int_{E_c}^{E_0} \frac{Q}{S^*} dE} \tag{3.5}$$

where, Q is the ionization cross-section (Eqn. 2.9), and R and S marked by * are for the specimen (unmarked R and S are for the standard). The back-scattering factor, R_i, varies both with the atomic number and the overvoltage (U). As the overvoltage decreases toward unity, fewer electrons with energies greater than E_c are back-scattered and hence, more electrons are available to cause ionization. R_i is expressed as:

$$R_i = \Sigma_j \; C_j R_{ij} \tag{3.6}$$

where, j represents the elements present in the standard or the specimen. Yakowitz et al. (1973) express R_{ij} as:

$$R_{ij} = R'_1 - R'_2 \ln (R'_3 \; Z_j + 25) \tag{3.7}$$

where,

$$R'_1 = 8.73\mathbf{x}10^{-3} \; U^{3} - 0.1669 \; U^{2} + 0.9662 \; U + 0.4523 \tag{3.8}$$

$$R'_2 = 2.703\mathbf{x}10^{-3} \; U^{3} - 5.182\mathbf{x}10^{-2} \; U^{2} + 0.302 \; U - 0.1836 \tag{3.9}$$

$$R'_3 = (0.887 \; U^{3} - 3.44 \; U^{2} + 9.33 \; U - 6.43) / U^{3} \tag{3.10}$$

The stopping power, S_i, is expressed as:

$$S_i = \Sigma_j \; C_j S_{ij} \tag{3.11}$$

where, j represents the elements present in the standard or the specimen. Thomas (1964) approximates the mean energy E_m as $(E_0+E_c)/2$ (see Eqns. 2.10-2.12) and calculates S_{ij} as:

$$S_{ij} = (\text{const}) \frac{2\left(\frac{Z_j}{A_j}\right)}{(E_0+E_c)} \ln\left(583 \frac{(E_0+E_c)}{J_j}\right) \tag{3.12}$$

where, E_0 and E_c are in keV, and J is in eV. The constant, and Q (also a constant) cancel out in the expression for $\mathbf{Z}_i$ (Eqn. 3.5). Furthermore, avoiding the integration, $\mathbf{Z}_i$ can be approximately expressed as:

$$\mathbf{Z}_i = \frac{(R_i S_i^*)}{(R_i^* S_i)} \tag{3.13}$$

To demonstrate the effect of atomic number difference between the specimen and the standard, the atomic number correction is calculated with the above equations for a complete range of Cu-Al alloys with respect to metal standards (Z_{Al}=13, Z_{Cu}=29) and a θ-phase (CuAl$_2$; average atomic number, Z=21.6) standard. There is a large atomic number difference for Cu between the specimen and the Cu standard in the Cu$_{10wt\%}$Al$_{90wt\%}$ alloy (C_{Cu}=0.1; Z=14.6). Hence, the atomic number correction for CuKα is also large ($\mathbf{Z}_{CuK\alpha}$ =1.149 at E_0=15 keV). The atomic number difference is small for Al in the same alloy. So, the correction for AlKα ($\mathbf{Z}_{AlK\alpha}$ =0.989 at E_0=15 keV) is also small. When the θ-phase is used as a standard for the same alloy, the atomic number difference for Cu decreases, whereas, it increases for Al. As a result, $\mathbf{Z}_{CuK\alpha}$ decreases to 1.045 (a decrease of ~60%) and $\mathbf{Z}_{AlK\alpha}$ increases to 1.038 under the same beam energy condition. An important conclusion from these graphs is that it is preferable to choose a standard with a composition similar to the specimen so that the magnitude of $\mathbf{Z}$ is small.
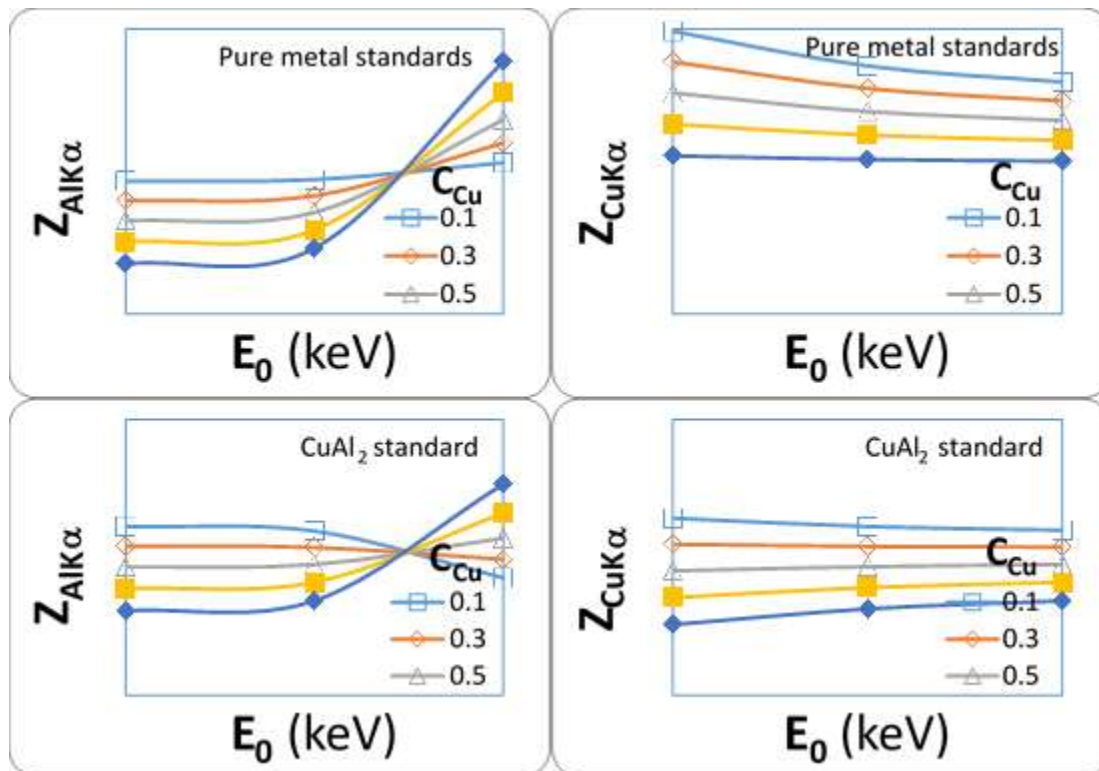
The crossover at ~17 keV of the $\mathbf{Z}_{AlK\alpha}$ values in the one of the graphs may be an artifact of the complex polynomial fit of the Duncumb & Reed data by Yakowitz et al.. Yakowitz's equations probably fail to work above a certain value of U, U_{Al}=9.62 (corresponding to E_0=15 keV) in this case. The relation between $\mathbf{Z}_i$ and U is complex, although in general, $\mathbf{Z}_i$ decreases very slowly with an increase in U. The uncertainty in $\mathbf{Z}_i$ does not change much as U increases. Since, as we will see later, high U values require large absorption corrections, a low U is preferable.

3.1.2. Absorption correction (A)

Not all primary generated x-rays are emitted from the specimen. Some of the x-rays generated at depth are absorbed in the specimen by interacting with other specimen atoms, which may become ionized as a result. The emitted intensity of element i is given as:
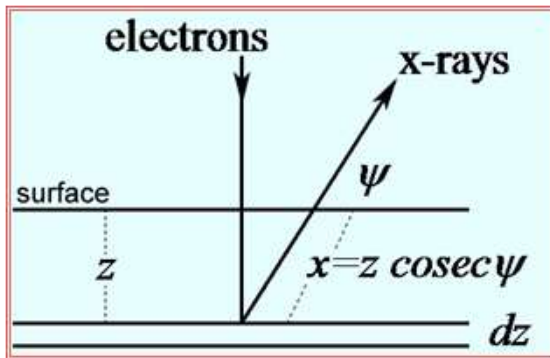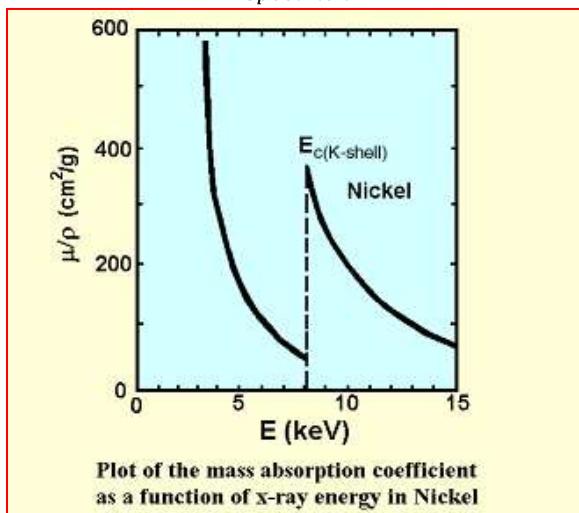
$$I_{i(emitted)} = I_{i(generated)}exp^{-\left(\mu/\rho\right)_{specimen}^{i-energy}(\rho x)}$$

(3.14)

where,

$$x = z\,cosec\,\psi$$

(3.15)

is the distance traveled by the x-ray inside the sample along an angle ψ (angle measured from the sample surface, also known as the *take-off angle*), z is the depth and the electron beam is perpendicular to the surface of the sample. $\left(\mu/\rho\right)_{specimen}^{i-energy}$ is known as the *mass absorption coefficient* (cm^2/g) of the specimen for the particular x-ray of element i.

The $\left(\mu/\rho\right)_{specimen}^{energy}$ of the specimen decreases with increasing incident x-ray energy, until the incident energy is slightly higher than an absorption edge (or critical excitation energy) of an element present in the specimen, where $\left(\mu/\rho\right)_{specimen}^{energy}$ jumps to a high value. This means that absorption is maximum when the energy of the x-ray is slightly above the critical excitation energy of the target atomic shell concerned. In the following example, ZnKα is absorbed by Ni because the energy of ZnKα (8.632 keV) is slightly higher than the critical excitation energy of the K-shell of Ni (E_c = 8.331 keV).

Plot of the mass absorption coefficient as a function of x-ray energy in Nickel

Energy	$E_{c(\text{K-shell})}$	$\left(\mu/\rho\right)_{Ni}^{energy}$
(keV)	(keV)	(cm^2/g)
CoKα 6.925		53
NiKα 7.472	**8.331**	60
CuKα 8.041		**49**
ZnKα 8.632		**311**

The total x-ray intensity emitted from an infinitesimal layer $d(\rho z)$ at a depth z can be expressed in terms of the depth-distribution function $\phi(\rho z)$ as:

$$dI'_i = \phi_i(\rho z)exp^{-\left(\mu/\rho\right)_{specimen}^{i-energy}(\rho z\, cosec\,\psi)}d(\rho z) \qquad (3.16)$$

where, $\phi_i(\rho z)d(\rho z)$ is the intensity of x-ray generated in the layer $d(\rho z)$. The total emitted intensity thus becomes,

$$I_{i(emitted)} = \phi_i(\Delta\rho z)\int_0^\infty \phi_i(\rho z)exp^{-\chi_i\rho z}d(\rho z) \qquad (3.17)$$

where,

$$\chi_i = \left(\mu/\rho\right)_{specimen}^{i-energy} cosec\,\psi \qquad (3.18)$$

The *absorption function*, $f(\chi_i)$, defined as the emitted fraction of the generated intensity, $I_{i(emitted)}/I_{i(generated)}$, is given by,

$$f(\chi_i) = \frac{\int_0^\infty \phi_i(\rho z)exp^{-\chi_i\rho z}d(\rho z)}{\int_0^\infty \phi_i(\rho z)d(\rho z)} \qquad (3.19)$$

The absorption correction $\mathbf{A}_i$ for an element i in a compound is given by:

$$\mathbf{A}_i = \frac{f(\chi_i)}{f(\chi_i)^*} \qquad (3.20)$$

where, the specimen is noted by *. Philibert (1963) modeled the absorption function $f(\chi_i)$ semi-empirically as:

$$f(\chi_i) = \left[\left(1+\frac{\chi_i}{\sigma_i}\right)\left(1+\frac{\chi_i}{\sigma_i}\frac{h_i}{1+h_i}\right)\right]^{-1} \qquad (3.21)$$

where,

$$h_i = 1.2\frac{A_i}{Z_i^2} \qquad (3.22)$$

and

$$\sigma_i = 4.5 \times 10^5 \frac{1}{\left(E_0^{1.65} - E_{c(i)}^{1.65}\right)} \tag{3.23}$$

σ, which takes into account the accelerating voltage and the critical excitation energy, is known as the Lenard coefficient and its formulation is given by Duncumb & Shields (1966) and Heinrich (1969). For compounds, the value of h, and $\left(\mu/\rho\right)_{specimen}^{energy}$ are evaluated as follows:

$$h_i = \sum_j h_j\, C_j \tag{3.24}$$

$$\left(\mu/\rho\right)_{specimen}^{i-energy} = \Sigma_j \left(\mu/\rho\right)_{element\ "j"}^{i-energy} C_j \tag{3.25}$$

Philibert obtained his equation by empirically fitting $\phi(\rho z)$ function of elements available at that time, but simplified the fit by setting $\phi_0 = 0$ (the value of $\phi(\rho z)$ at the surface). However, ϕ_0 is always >1 due to scattering of back-scattered electrons within the sample. Hence, in cases where most of the x-rays are generated near the surface (e.g., light element (C,N,O) x-rays in a metal matrix (Ti,Fe,Cu)), the Philibert equation produces erroneous results.

The absorption correction is a function of the mass absorption coefficients, the take-off angle and the accelerating voltage. To understand the effect of these three parameters on the absorption correction, the Mg-Al binary alloy is considered. AlKα (E_K=1.487 keV) is highly absorbed in Mg ($E_{c(K-shell)}$=1.303 keV) with $\left(\mu/\rho\right)_{Mg}^{AlK\alpha}$ = 4168 cm^2/g. The following plots show calculated absorption corrections for AlKα (using E_c from Bearden, 1964 and (μ/ρ) from Heinrich, 1986) for different compositions of the Mg-Al alloy under different E_0 and ψ conditions. Three conclusions emerge from these plots: the absorption correction, $\mathbf{A}_{AlK\alpha}$, increases with increasing operating voltage, decreasing take-off angle and increasing Mg in the specimen. Shorter distances traveled by a primary x-ray within the sample lessens its absorption. Therfore, higher take-off angles and lower operating voltages lead to a lower absorption correction. Also, more Mg in the sample leads to a more efficient absorption of the AlKα. Most electron microprobes have fixed take-off angles. Hence, a low overvoltage should be used to minimize the absorption correction.
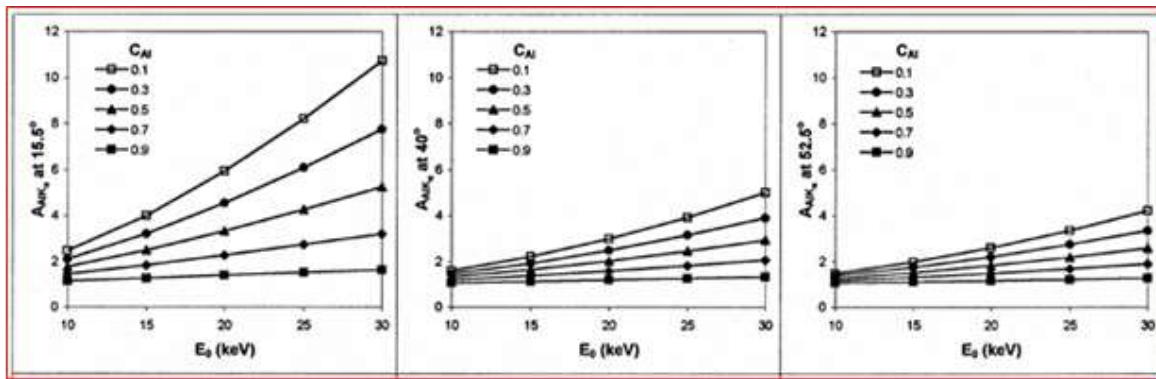
The error in the mass absorption coefficient propagates into the final result. The effect of uncertainties in mass absorption coefficients is low when the value of the absorption function $f(\chi)$ is greater than 0.7.

3.1.3. Characteristic fluorescence correction (F)

X-ray fluorescence occurs as a consequence of photoelectric absorption of primary x-rays as the target atom relaxes from an excited state. These secondary x-rays may be generated both by characteristic or continuum x-rays. Since x-rays can travel longer distances than electrons in matter, the *range for fluoresced x-rays is also greater than the primary electron interaction range*. The secondary x-ray interaction volume may be as much as 1000 times greater than the primary interaction volume.

Element	$E_{K\alpha}$	$E_{K\beta}$	$E_{c(K\text{-shell})}$	$\left(\mu/\rho\right)^{NiK\alpha}_{Absorber}$
(Atomic No.)	(keV)	(keV)	(keV)	(cm^2/g)
Mn(25)	5.895	6.492	**6.537**	**344**
Fe(26)	6.4	7.059	**7.111**	**380**
Co(27)	6.925	7.649	7.709	53
Ni(28)	**7.472**	8.265	**8.331**	59
Cu(29)	8.041	**8.907**	8.98	65.5

The data in the above table indicates that NiKα, with an energy of 7.472 keV, will be efficiently absorbed in Fe and Mn, whose K-shell critical excitation energies are 7.111 keV and 6.537 keV, respectively. As a result, both Fe and Mn (Kα and Kβ) will be fluoresced by NiKα. The table also shows that NiKα and Kβ can only be fluoresced by CuKβ because only CuKβ has an energy (8.907 keV) greater than the Ni K-shell absorption edge (8.331 keV). CuKβ will be absorbed in the process. The following table shows which x-rays will cause fluorescence in the different elements:

Element (Kα, Kβ)	Radiation causing fluorescence
Mn	FeKβ, CoKα, CoKβ, NiKα, NiKβ, CuKα, CuKβ
Fe	CoKβ, NiKα, NiKβ, CuKα, CuKβ
Co	NiKβ, CuKα, CuKβ
Ni	CuKβ
Cu	none

The fluorescence correction for element i in a compound of j elements is as follows:

$$\mathbf{F}_i = \frac{\left(1 + \Sigma_j\left\{I_{ij}^f/I_i\right\}\right)}{\left(1 + \Sigma_j\left\{I_{ij}^f/I_i\right\}\right)^*} \tag{3.26}$$

where, I^f_{ij} is the intensity of element i fluoresced by element j, and I_i is the primary x-ray intensity produced by the electron beam. For an elemental standard, the numerator reduces to unity. I^f_{ij}/I_i is given by Castaing (1951) and modified by Reed (1965) as:

$$I^f_{ij}/I_i = C_j Y_0 Y_1 Y_2 Y_3 P_{ij} \qquad (3.27)$$

where,

$$Y_0 = 0.5\left(\frac{r_i - 1}{r_i}\right)\left(\omega_j \frac{A_i}{A_j}\right) \qquad (3.28)$$

where, r_i is the absorption edge jump-ratio; $\left(\frac{r_i-1}{r_i}\right)$ is 0.88 for K-line, 0.75 for L-line; and ω_j is the fluorescent yield,

$$Y_1 = \left(\frac{U_j - 1}{U_i - 1}\right)^{1.67} \qquad (3.29)$$

$$Y_2 = \frac{\left(\mu/\rho\right)^j_i}{\left(\mu/\rho\right)^j_{spec}} \qquad (3.30)$$

where, $\left(\mu/\rho\right)^j_i$ and $\left(\mu/\rho\right)^j_{spec}$ are the mass absorption coefficients for x-rays from element j in element i and the specimen, respectively,

$$Y_3 = \frac{\ln(1+u)}{u} + \frac{\ln(1+v)}{v} \qquad (3.31)$$

where,

$$u = \frac{\left(\mu/\rho\right)^i_{spec}}{\left(\mu/\rho\right)^j_{spec}} \operatorname{cosec}\psi \qquad (3.32)$$

and

$$v = 3.3\text{x}10^5 \frac{1}{\left(E_0{}^{1.65} - E_c{}^{1.65}\right)\left(\mu/\rho\right)^j_{spec}} \qquad (3.33)$$

and, P_{ij} is a factor for the type of fluorescence occurring. For K x-ray fluorescing another K x-ray, $P_{ij}=1$; for K fluorescing L, $P_{ij}=4.76$; for L fluorescing K, $P_{ij}=0.24$).

The fluorescence correction thus depends on absorption edge jump-ratio (r), the fluorescent yield (ω) of the fluorescer x-ray, mass absorption coefficients, the take-off angle and the operating voltage. To understand the effect of ψ and E_0 on the fluorescence correction, the Mg-Al binary alloy is again considered. Since AlKα (E_K=1.487 keV) is highly absorbed in Mg ($E_{c(K\text{-shell})}$=1.303 keV) and $E_K{}^{AlK\alpha} > E^{Mg}_{c(K\text{-shell})}$, MgK$\alpha$ will be fluoresced. Using the above equations, ω from Bambynek et al. (1972), (μ/ρ) from Heinrich (1986) and E_c from Bearden (1964), $\mathbf{F}_{MgK\alpha}$ in a range of Mg-Al compositions is calculated under different ψ and E_0 conditions. The plots show that $\mathbf{F}_{MgK\alpha}$ increases with increasing E_0 and Al-content of the specimen. Changing ψ does not have a significant effect

on the correction. A high ψ is preferred because it minimizes the absorption correction. Also, the error in the fluorescence correction is low at low ψ and does not increase at high ψ. Therefore, a low E_0 and high ψ angle is recommended.
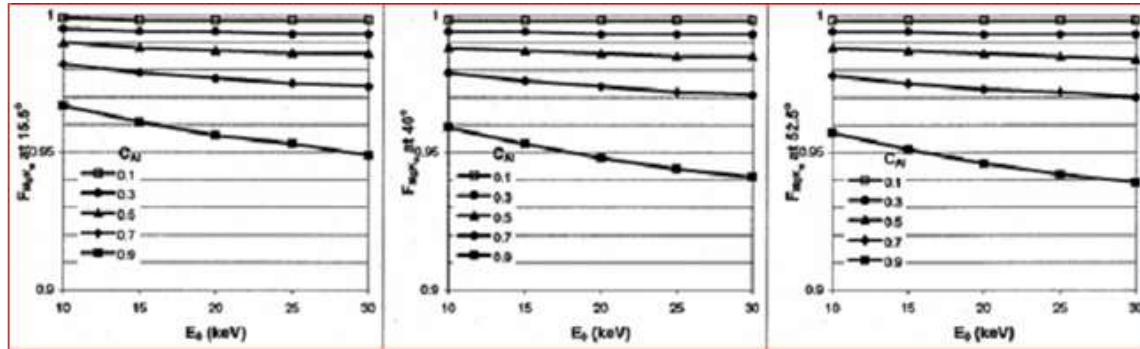
3.1.4. Continuum fluorescence correction

Energy of continuum x-rays range between 0 keV and E_0. When the energy of the continuum x-rays is greater than the critical excitation energy of an atomic shell of an element in the specimen, the element is fluoresced. Thus, continuum x-rays with energies between E_c and E_0 cause fluorescence and the fluorescence effect of all energies between E_c and E_0 must be considered in continuum fluorescence correction. Myklebust et al. (1979) concluded that continuum induced fluorescence may be ignored if $f(\chi) < 0.95$, $C_i > 0.5$ and Z_{std} (atomic number) is similar to Z_{spec}. By choosing a low overvoltage and a high take-off angle continuum fluorescence correction can be avoided except while analyzing a heavy component in a light matrix (e.g., U in a common silicate mineral) when $f(\chi) > 0.95$. In such a case, a low energy characteristic x-ray of the element should be analyzed (e.g., U$M\alpha$).

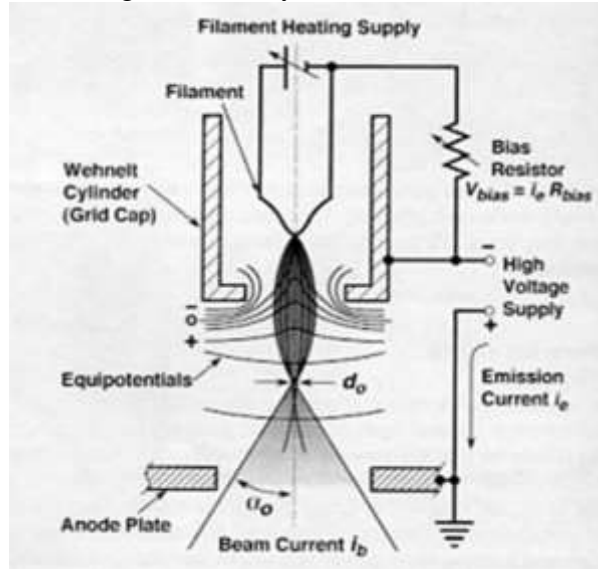### 3.1.5. The $\phi(\rho z)$ correction procedure

The $\phi(\rho z)$ correction procedure uses experimentally measured depth-distribution of x-rays to model the atomic number and the absorption corrections with a single expression. The equations for generated and emitted x-ray intensities (Eqn. 2.14 and 3.14) are combined:

$$\mathbf{Z_i A_i} = \frac{\int_0^\infty \phi_i(\rho z)\exp^{-\chi_i \rho z}d(\rho z)}{\int_0^\infty \phi_i^*(\rho z)\exp^{-\chi_i^* \rho z}d(\rho z)} \qquad (3.34)$$

and modeled empirically in terms of α, β, γ and ϕ_0 (Packwood and Brown, 1981), or semi-empirically in terms of ϕ_0, R_m, R_x and the integral of the $\phi(\rho z)$ distribution (Pouchou and Pichoir, 1984). The fluorescence correction is calculated separately with the Castaing-Reed method (Eqn. 3.26) and combined with Eqn. 3.34 to obtain the full ZAF correction.
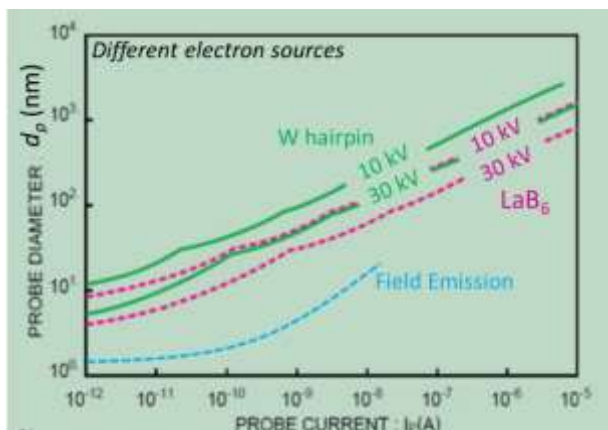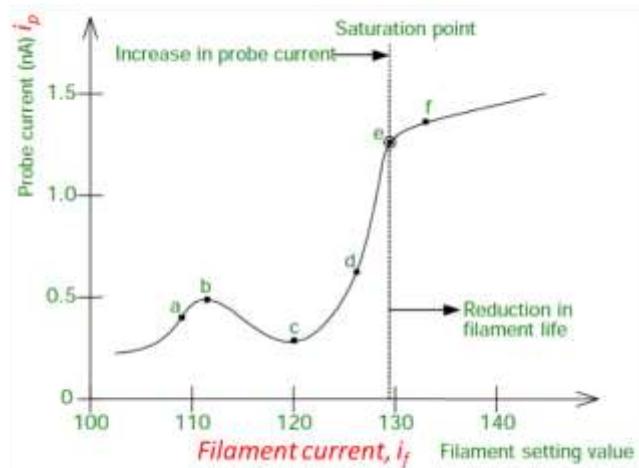
4. THE ELECTRON SOURCE IN ELECTRON MICROPROBE

A common source for the electron beam is a tungsten hairpin filament. A typical electron gun assembly is known as a "self-biased triode thermionic emitter". The cathode consists of the tungsten hairpin maintained at a negative potential. Tungsten has a high melting point and low work-function energy barrier, i.e., the energy required to extract electrons to be emitted. The filament is heated by filament current, i_f, until electrons overcome barrier. The anode plate is at ground potential. The potential difference (accelerating voltage, V_0) between the anode plate and the filament accelerates the electrons and causes emission with emission current, i_e. The filament is covered by a grip cap known as the Wehnelt cylinder. The grid cap is at a slightly more negative potential than the filament. The voltage different is maintained by a bias resistor, and the bias voltage (V_{bias}) varies automatically with fluctuations in i_e to stabilize emission. The grid cap also focuses the electron beam to an initial diameter, d_0, divergence angle, α_0, and beam current, i_b. When V_{bias} is optimum, the zero equipotential surface just touches the filament tip and emission is optimal. If V_{bias} is too high, there is no emission. If it is too low, emission is high but focusing is poor. The beam travels through several lenses and apertures to produce a final beam current (probe current), i_p, a final beam diameter (probe diameter), d_p, and a final beam convergence angle (probe convergence angle), α_p. The filament is saturated by slowly increasing the filament current until the probe current reaches a stable value known as the saturation point. The probe diameter decreases as probe current decreases and accelerating voltage increases. It also depends on the source

and decreases with W hairpin > LaB_6 > Field emission source. The probe current can be adjusted using the condenser lens control and the objective lens aperture settings.

With typical operating conditions of 15 kV accelerating voltage and 10 nA probe current, the probe diameter is ~100 nm. However, the lateral diameter of the beam interaction volume is always larger than the beam diameter, and the spatial resolution of analysis is poorer.

Monte Carlo simulations of electron trajectories in the sample
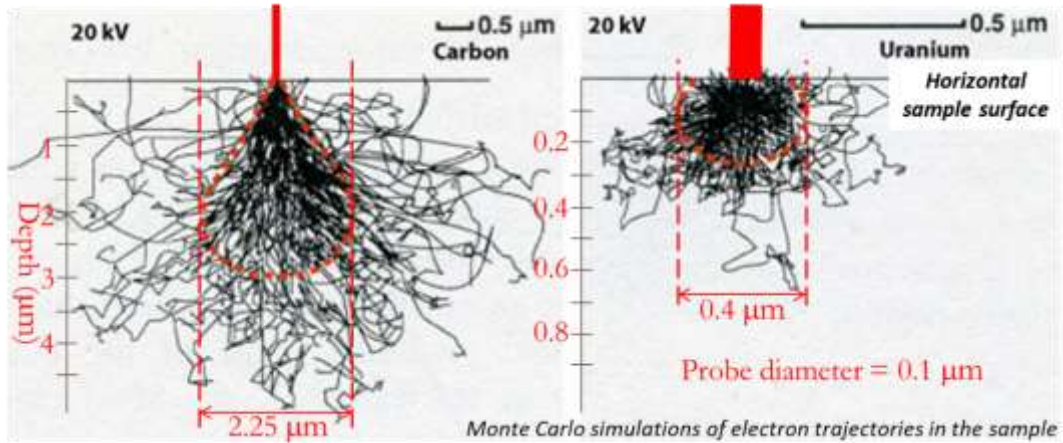
The probe convergence angle determines the depth of focus.
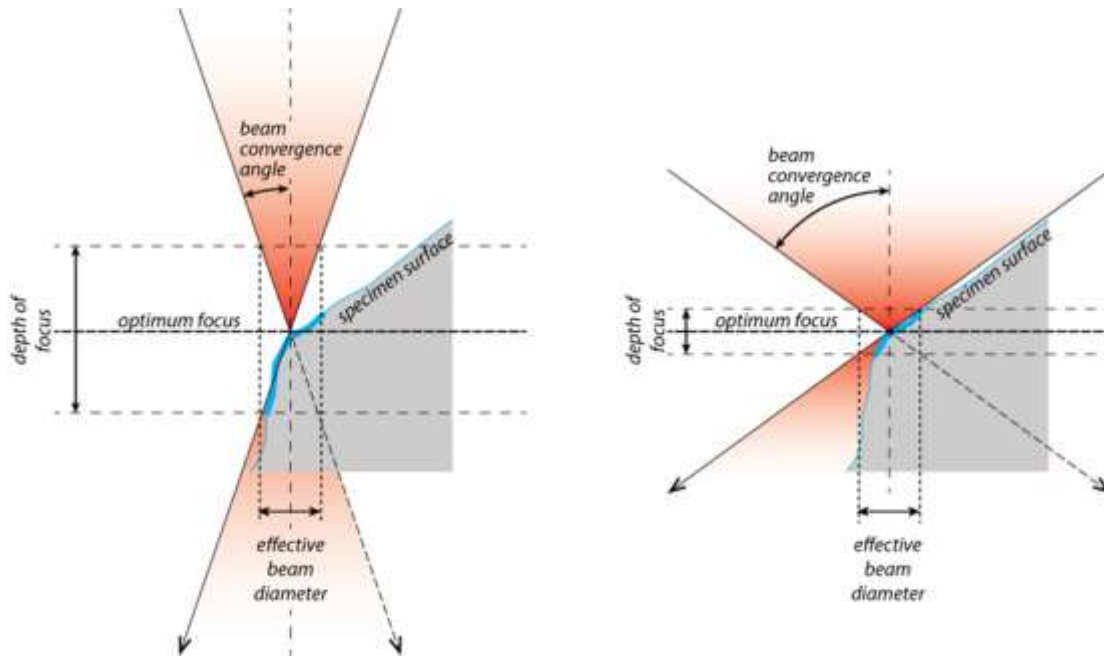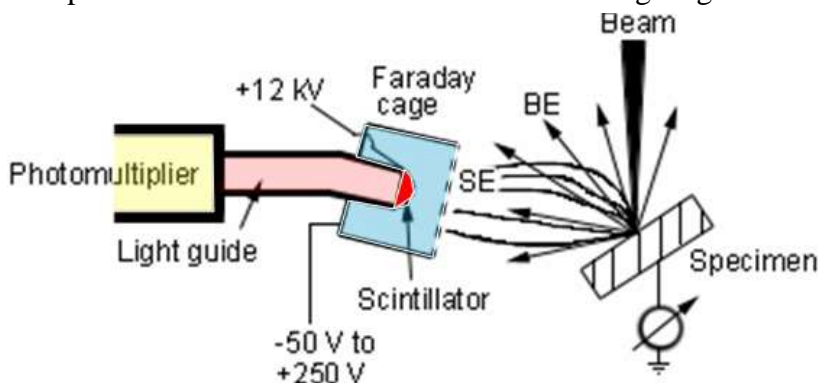
5. DETECTORS IN THE ELECTRON MICROPROBE

The electron microprobe can be used to obtain high resolution images by rastering the electron beam over the specimen surface. The signal is plotted on the display monitor as the beam scans to form the image. Depending on the signal, the image can be a backscattered or secondary electron image, an elemental x-ray map or a cathodoluminescence image. The elemental maps can be obtained with the EDS or WDS.
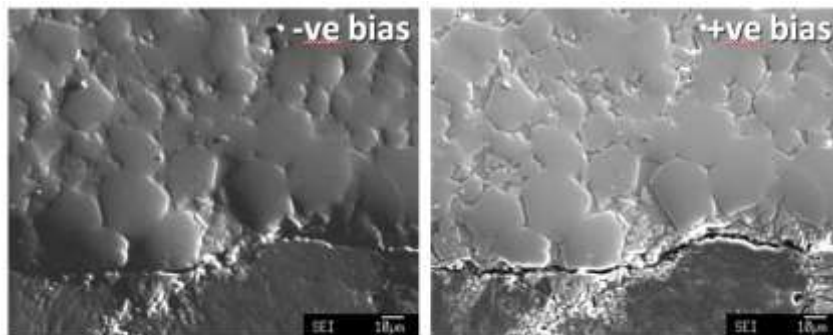
5.1. ELECTRON DETECTORS

Back-scattered electrons have energies between 0 keV and E_0. In contrast, secondary electrons have energies in the range 0-50 eV, mostly between 3 and 5 eV. Therefore, different detectors are required to detect the two electron signals.

5.1.1. Everhart-Thornley (E-T) secondary electron detector

The E-T detector consists of a scintillator maintained at a high positive potential of +12 kV to attract the incoming electrons. The electrons interact with the scintillator and produce light that travels through a light guide, a solid plastic or glass rod, to a photomultiplier, which in turn produces electric current that forms the image signal. The scintillator is enclosed in a Faraday cage which can be biased to a negative or positive potential (-50 to +250 V). When the E-T detector is negatively biased, only the high energy backscattered electrons are able to enter the detector. Because the E-T detector is mounted on the side wall of the sample chamber, it receives a highly directional view of the specimen, and only the facets of a rough surface directly in the line-of-sight appear bright. When the E-T detector is positively biased, it intercepts both backscattered and secondary electrons. The trajectories of secondary electrons produced on the facets not in line-of-sight are bent and pulled into the detector, and all facets look illuminated. The E-T detector is thus a useful tool for topographic imaging.

5.1.2. Solid-state diode backscattered electron detector
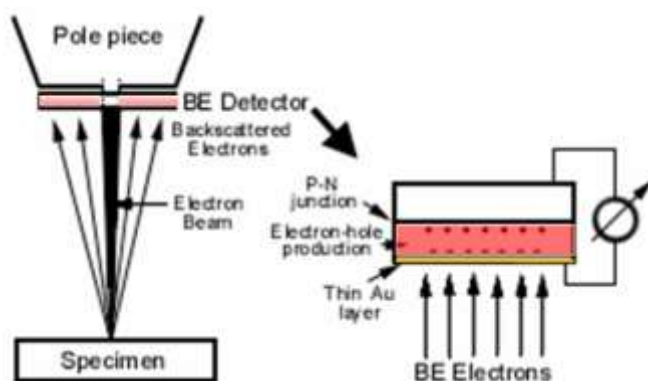
The solid-state diode detector is a semiconductor that tracks changes in voltage caused by variable electron-hole production from interactions with backscattered electrons as the beam scans over the specimen. It is a flat, annular wafer mounted on the pole-piece of the objective lens. The annular detector is split into two semi-circular parts, A and B. When signal from both parts are added (A+B mode), good compositional contrast is obtained. The A-B mode is analogous to a stereoscopic view that produces topographic contrast.
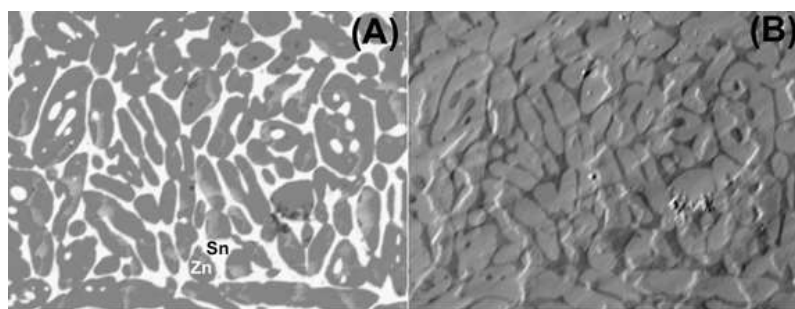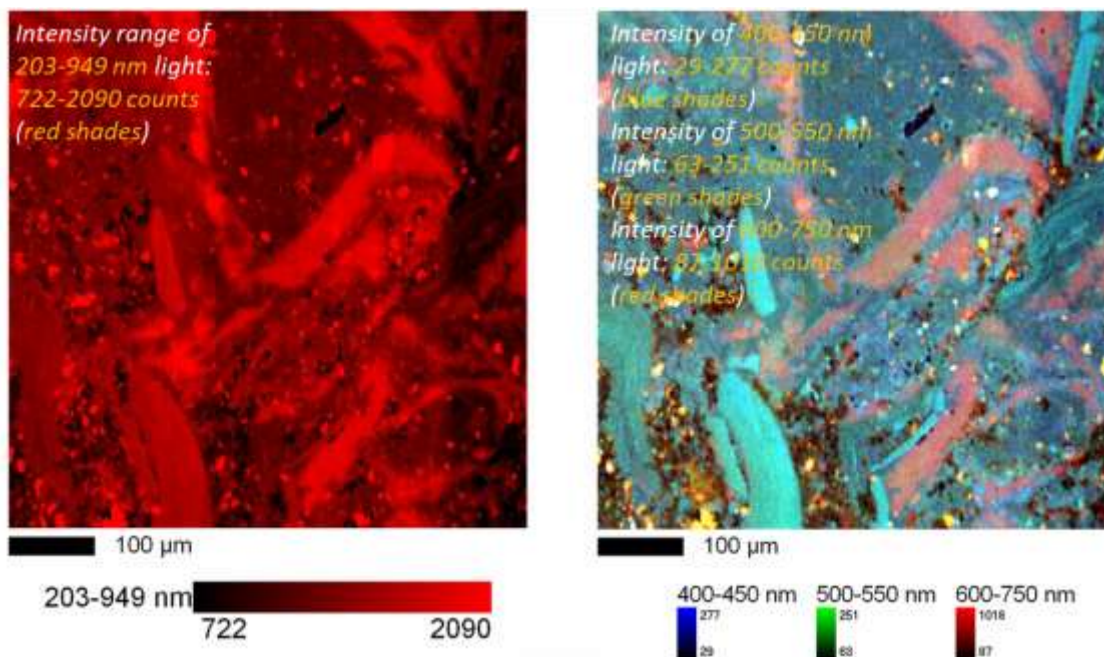

Scanning backscattered electron images of a Zn-Sn composite collected through a solid-state diode detector in (A) A+B, or compositional mode; (B) A-B, or topographic mode

5.2. CATHODOLUMINESCENCE DETECTOR

On an electron microprobe, cathodoluminescence (CL) is detected by a CCD-type detector attached to the optical microscope port with a fiber optic cable.
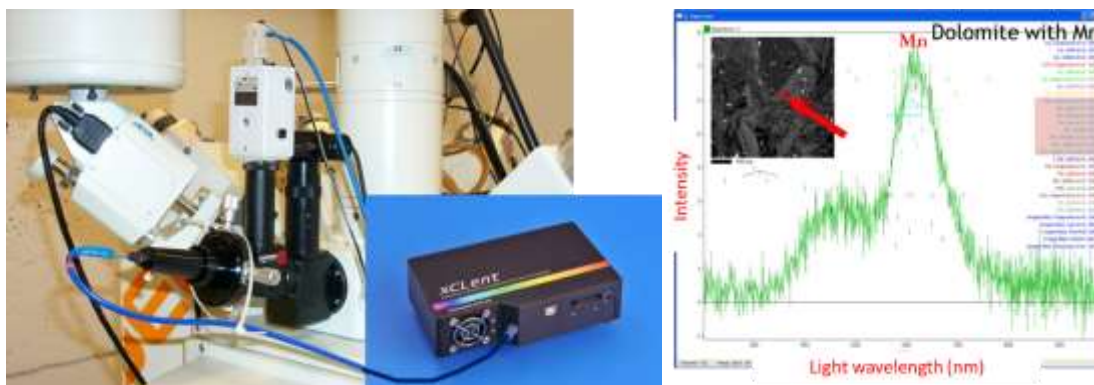
Spectrometry and imaging may be carried out with the light signal. Hyperspectral CL images with a continuous visible light spectrum collected at each pixel of the image can be displayed in greyscale mode, single or multi-channel false color mode where the greyscale or color scale indicates the intensity of the light signal.

Intensity range of 203-949 nm light: 722-2090 counts (red shades)

Intensity of 400-450 nm light: 29-277 counts (blue shades)
Intensity of 500-550 nm light: 63-251 counts (green shades)
Intensity of 600-750 nm light: 87-1016 counts (red shades)

100 µm

100 µm

203-949 nm   722   2090

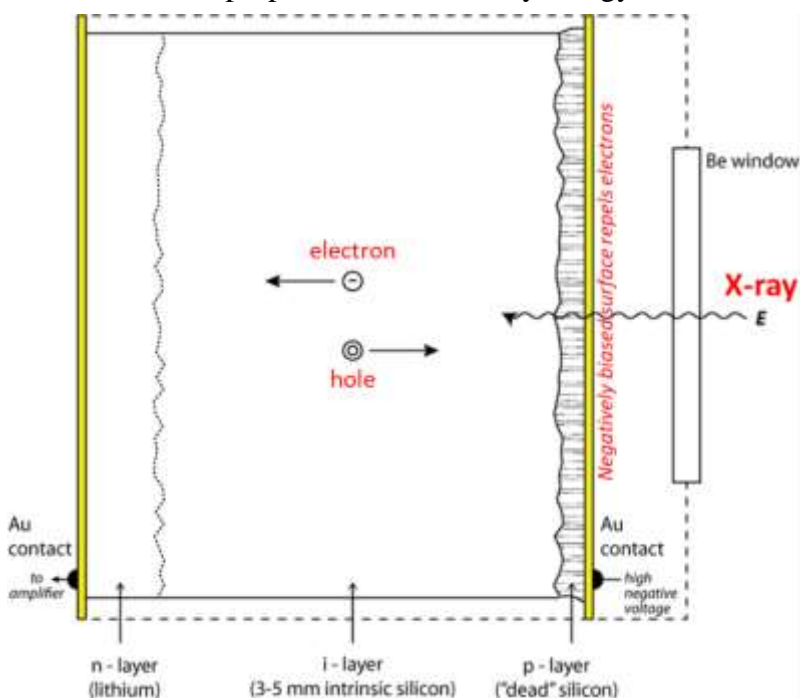400-450 nm   277 / 29   500-550 nm   251 / 63   600-750 nm   1016 / 87

5.3. X-RAY DETECTORS

An electron microprobe is usually equipped with an energy dispersive spectrometer (EDS) and several wavelength dispersive spectrometers (WDS) for x-ray spectrometry.

### 5.3.1. Energy dispersive spectrometer (EDS)

An energy dispersive spectrometer (EDS) takes advantage of the phenomenon of electron-hole production by incident x-rays in a semiconductor. Electric current produced in the detector is proportional to the x-ray energy. A multichannel analyzer (MCA) is used to analyze the electrical pulses and construct an x-ray spectrum for the entire energy range (0 keV to E_0). Elements down to Be ($Z=4$) can be detected with a windowless detector.

Pure Si is a semiconductor and a good material for a detector. However, Si usually contains some B as impurity that creates holes in the valence band of Si. This electron deficiency makes Si a conductor. Since B is a p-type dopant, an n-type

electron ⊖

hole ◎

Be window

X-ray E

Negatively biased surface repels electrons

Au contact
to amplifier

Au contact
high negative voltage

n – layer (lithium)   i – layer (3-5 mm intrinsic silicon)   p – layer ("dead" silicon)

dopant such as Li is added to Si to compensate the electron deficiency created by B. Li is applied on the surface of Si and allowed to diffuse into the crystal. This forms a micrometer-thick p-n zone at the Si-Li interface that acts as an intrinsic semiconductor. A reverse voltage bias is applied at liquid nitrogen temperature to the p-n zone, which enlarges the intrinsic zone to a thickness of a few millimeters. Li is mobile under an applied bias at room temperature. Hence, a Si(Li) detector should always be operated at liquid-nitrogen temperatures to prevent damage.
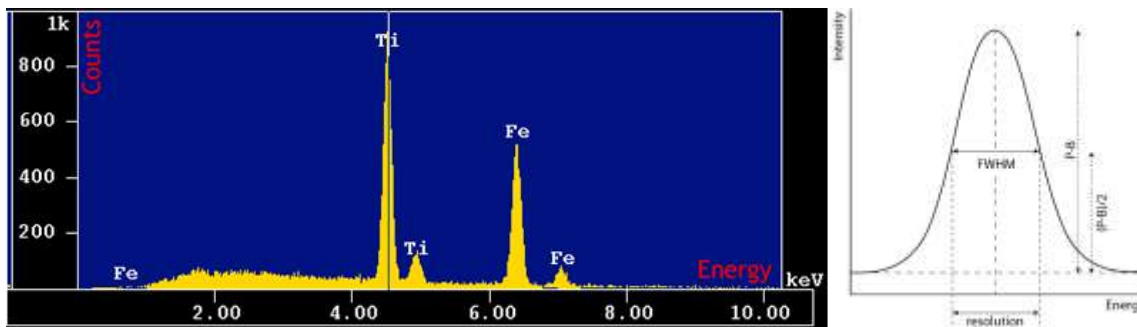

An x-ray spectrum acquired with the EDS shows characteristic peaks of elements and a continuum that forms the background signal. The energy resolution of a typical EDS is ~150 eV, measured at the full-width half-maximum (FWHM) of the MnKα peak.

## 5.3.2. Wavelength dispersive spectrometer (WDS)

A WDS system consists of two components: an analyzing crystal or diffractor, and an x-ray detector known as the proportional counter. WDS takes advantage of the Bragg diffracting characteristics of an analyzing crystal to preferentially diffract the wavelength of interest toward the detector. Bragg's law is:

$$n\lambda = 2d \sin\theta \qquad (4.1)$$
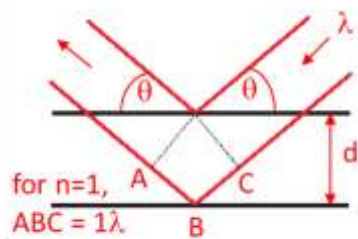
where, λ is the wavelength of the x-ray, d is the lattice spacing of the crystal, θ is the angle of incidence and diffraction, and n is the order of reflection. X-rays are reinforced after diffraction when the path lengths between two rays differ by an integer (n) multiplied by the wavelength (path ABC). Combined reflections from a large number of lattice planes result in a narrow intensity distribution around a peak. E.g., the FWHM energy interval of MnKα is about 10 eV compared to the natural value of 2 eV.

$$n\lambda_1 = 2d \sin\theta_1 \qquad\qquad n\lambda_2 = 2d \sin\theta_2$$
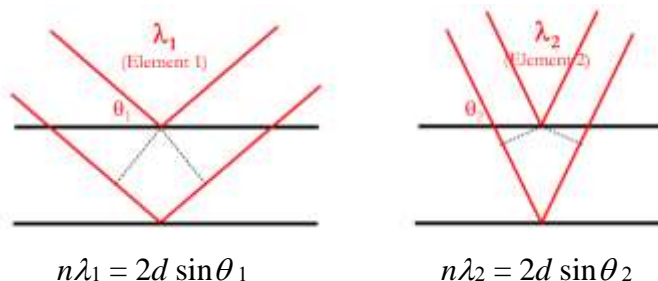
For the same order of diffraction (n), the wavelength being diffracted (λ_1, λ_2) changes with the incidence angle (θ_1, θ_2). However, by changing the incidence angle appropriately, different orders of the same wavelength can be diffracted. In this case, the length of path DEF is twice the length of path ABC, and sin $\theta_2 = 2\sin\theta_2$.

$$1\lambda_1 = 2d \sin \theta_1 \qquad\qquad 2\lambda_2 = 2d \sin \theta_2$$
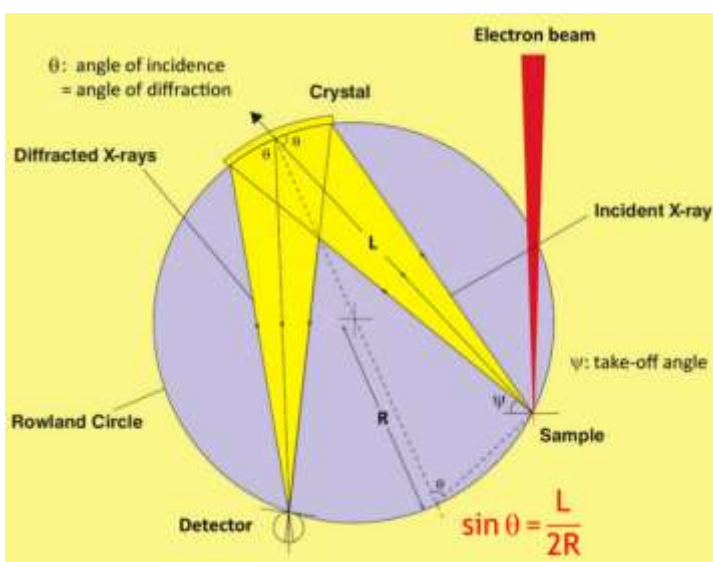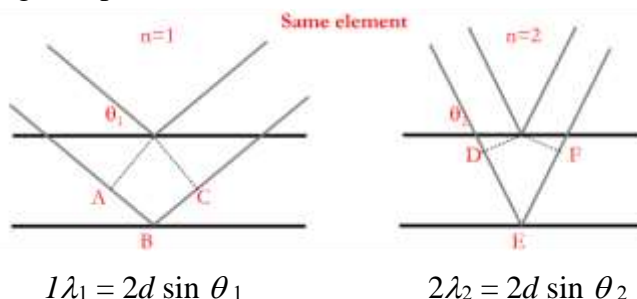
In WDS, the x-ray source (point of the sample from where x-rays are emitted), the analyzing crystal and the detector slit are positioned on the circumference of a focusing circle known (Rowland circle). From the geometrical relation $\sin\theta = \frac{L}{2R}$ and Bragg's law, λ is related to L, the distance between the sample and the analyzing crystal, by the following relation:

$$L = n\lambda \frac{R}{d} \qquad (4.2)$$

(mm), where, R is the radius of the focusing circle (e.g., 140 mm or 100 mm).

In a Johansson-type spectrometer, the crystal is bent to a radius of curvature of 2R and then ground to R. The diffracted x-rays are thus fully focused into the detector. Alternatively, crystals are only bent but not ground. This compromise, known as Johann optics, does not seriously impair the spectrometer resolution. A good quality Johansson-type spectrometer has a FWHM spectral resolution of ~10 eV. This is an order of magnitude better than a typical EDS that has a FWHM resolution of ~150 eV. As a

Vertical scale for EDS
exaggerated for comparison
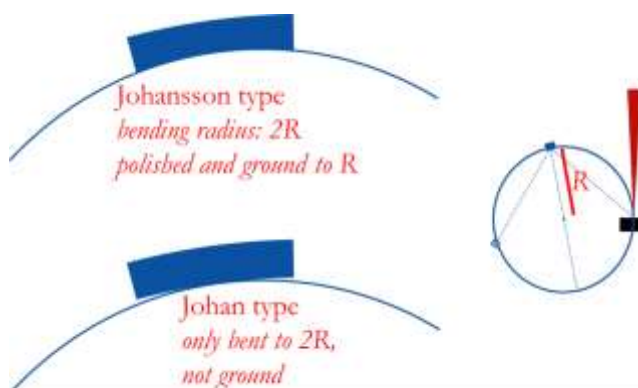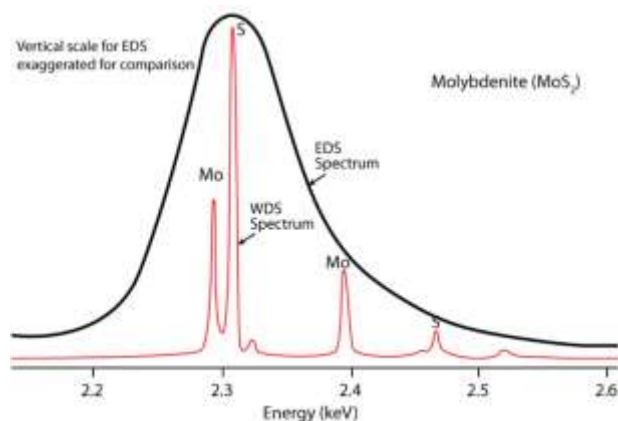
Molybdenite (MoS₂)

result, peak overlaps in compounds such as molybdenite (MoS_2) that cannot be resolved with the EDS are easily resolved with the WDS.

To detect different x-ray wavelengths, the crystal is moved in a straight line toward or away from the sample at an angle, ψ (take-off angle), the angle between the specimen-surface and the x-ray travel direction. The take-off angle is fixed by the design of the instrument. As the crystal moves, it also rotates so that the x-ray incidence angle, θ, changes. As a result, different wavelengths are diffracted. The detector moves simultaneously so that it remains in path of the diffracted x-rays. The focusing circle changes position, but its size remains the same.

$$n\lambda_1 = 2d \sin \theta_1$$

$$L_1 = n\lambda_1 . R/d$$

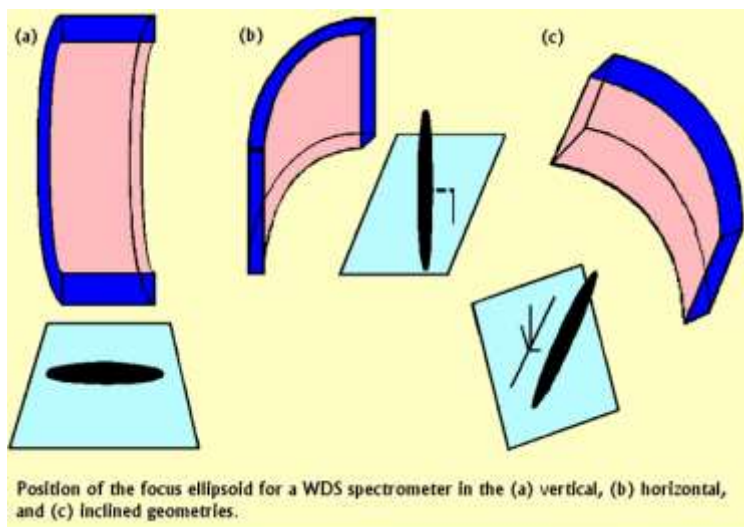$$n\lambda_2 = 2d \sin \theta_2$$

$$L_2 = n\lambda_2 . R/d$$
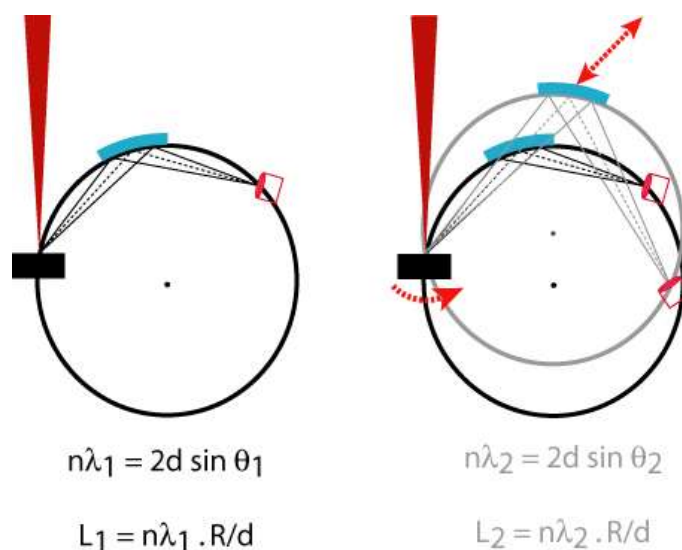
5.3.2.1. *Diffracting crystals in WDS*

Because of the geometrical characteristics of WDS, x-rays emitted from only a small elliptical volume of the sample reaches the detector. The shape of this x-ray focus volume depends on the shape of the analyzing crystal and is usually an elongated ellipsoid. The major axis of the focusing ellipsoid is proportional to the width of the diffracting crystal and has a length of several millimeters.

In electron microprobes, WD spectrometers are usually mounted vertically so that the focusing circle is vertical. In this configuration, the major axis of the focusing ellipsoid is horizontal and in the plane of the specimen-surface. A small movement of the specimen in the vertical direction may move the surface outside the focusing ellipsoid and the emitted x-rays will fail to reach the detector. Therefore, the surface is always focused with an optical microscope coaxial with the electron beam during an analytical session. The optical microscope has a fixed focus and the surface can be focused accurately. During maintenance, the spectrometer is slowly moved up or down while the surface is in optical

focus until the x-ray counts are maximized, ensuring that the major axis of the focusing ellipsoid is on the specimen-surface. At the start of an analytical session, the surface is focused both with the optical microscope and the objective lens-controls of electron beam. This ensures that the specimen-surface is in x-rays focus when it is in optical focus.

Position of the focus ellipsoid for a WDS spectrometer in the (a) vertical, (b) horizontal, and (c) inclined geometries.

The primary x-ray production volume is much smaller than the volume of the focusing ellipsoid. Since x-ray fluorescence may occur from a much larger volume than the primary x-ray volume, a vertical spectrometer will intercept a significant amount of the fluoresced x-rays. This is a minor problem in a horizontal or inclined spectrometer. However, such configurations require low x-ray take-off angles to maximize the x-ray signal in the detector (e.g., in the horizontal configuration, the Rowland circle is also horizontal). Because of absorption and fluorescence correction issues, low take-off angles are not recommended.
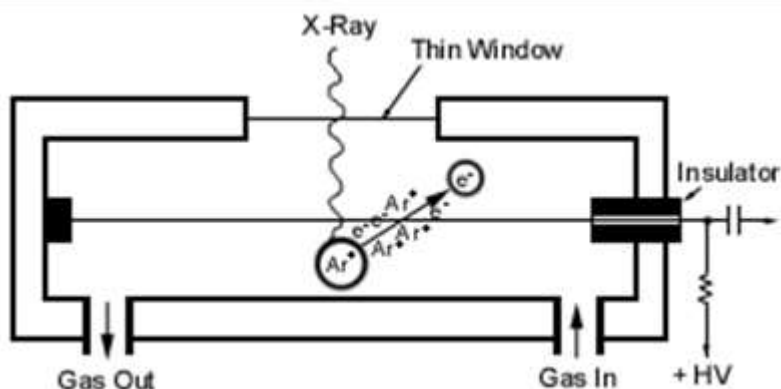
Analyzing crystals layered diffractors commonly available and elements commonly analyzed with them are as follows:

*5.3.2.2. X-ray detector in WDS: proportional counter*

The commonly used detector in WDS is known as a proportional counter. It consists of a gas filled tube with a thin tungsten wire along its axis maintained at a potential of 1-3 kV. The counter is either sealed or a gas-flow type. In a flow counter, gas flows through the tube. X-rays enter the tube through a thin window and ionize the gas atoms. Depending on the voltage in the wire, the electron ejected from the gas atom may ionize other gas atoms. The electrons are collected by the wire, creating a signal pulse whose voltage is proportional to the applied potential in the wire. The signal is amplified, filtered, and counted by the electronics.

Because one ionization in the gas can set off a chain of ionizations, the signal is amplified internally in the counter, resulting in count rates of 0-50,000 counts per second. The gas amplification factor, a measure of the internal amplification, is proportional to the applied potential in the wire within a range of approximately 1.6-1.8 kV.

The type of gas depends on the wavelength of the x-ray to be detected.
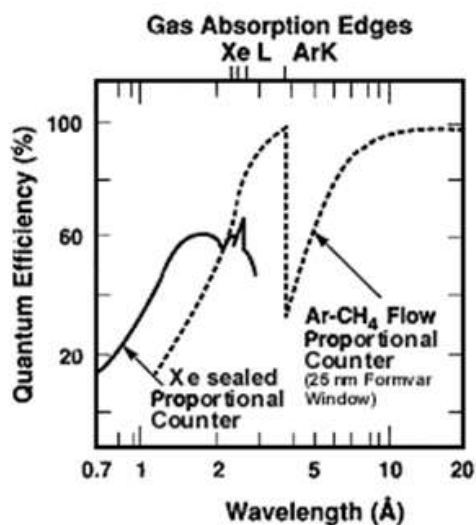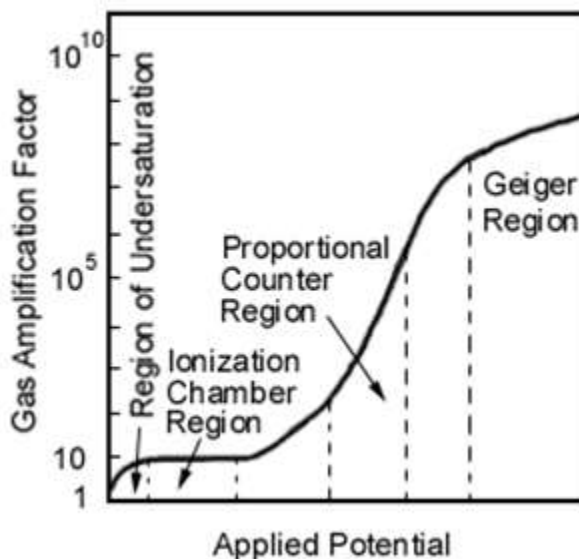
The efficiency of detection, measured as quantum efficiency, of Xe is greater than that of Ar for short wavelength x-rays. Since the LIF and PET crystals are appropriate for short wavelength detection, these crystals are usually combined with sealed Xe-counters. The quantum efficiency of P-10 gas (Ar diluted with 10% methane, a quenching agent) is greater for long wavelength x-rays. Hence, gas-flow proportional counters are usually combined with TAP or LDE for light element detection. When the x-ray entering the detector has enough energy, E_{x-ray}, to ionizes the Ar K-shell or Xe L-shell (i.e., when
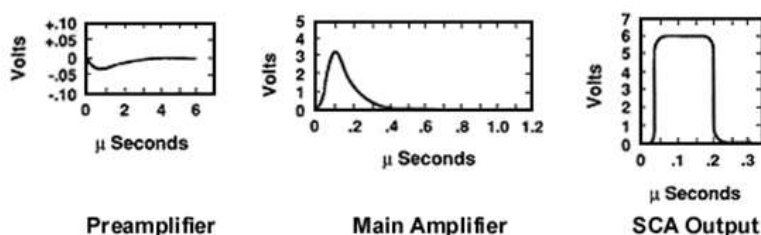
overvoltage $U = \frac{E_{X\text{-}ray}}{E_{c(Ar\ K\text{-}shell)}}$ or $\frac{E_{X\text{-}ray}}{E_{c(Xe\ L\text{-}shell)}}$ is > 1), the incoming x-ray is absorbed and ArKα or XeLα is fluoresced. Thus, there is sharp drop in the quantum efficiency. The efficiency of an Ar-counter may be improved by increasing the gas pressure to 2-3 atmospheres.

The thin window on a sealed Xe-counter is made of Be. The window material on a flow Ar-counter is usually an organic compound such as formvar or polypropylene. Each material has its own x-ray transmittance property. The thickness of the film also determines the amount of x-ray that can be transmitted. E.g., a 1 μm thick polypropylene window transmits more x-rays than a 6 μm thick polypropylene window.
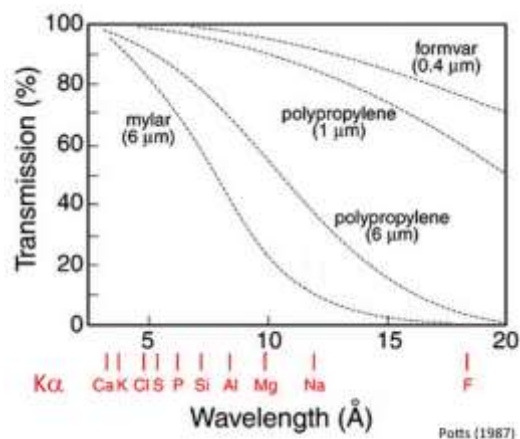
5.3.2.3. *Signal processing in WDS: pulse height analysis (PHA)*

The signal generated in the proportional counter passes through a preamplifier to produce a small negative voltage pulse. In turn, this pulse passes through the main amplifier that inverts, amplifies and shapes the pulse such that its voltage has Gaussian distribution. From the main amplifier, the pulses enter the single channel analyzer (SCA).The

Typical WDS x-ray detection pulse shapes

SCA selects pulses within a preset voltage range and produces fixed rectangular pulses of a fixed voltage and duration compatible with scalar and rate-meter input requirements of the digital counting system. Selection of pulses within a predetermined voltage range is known as pulse-height analysis (PHA). A baseline, E_L, and a window voltage, ΔE, are set such that any voltage pulse outside this voltage range is rejected by the SCA. In the example shown in the figure, only pulses between 5 and 7 eV (pulse II) are accepted. To determine E_L and ΔE an SCA scan is employed. The pulse-voltage distribution is obtained by selecting a small window voltage (ΔE of a few tenths of a volt) and slowly moving the window over the SCA voltage range (0-10 V).

The voltage of the output pulse from the amplifier is directly proportional to the energy of the x-ray that entered the proportional counter. E.g., the energy of SiKα (1.739 keV) is ~1.4
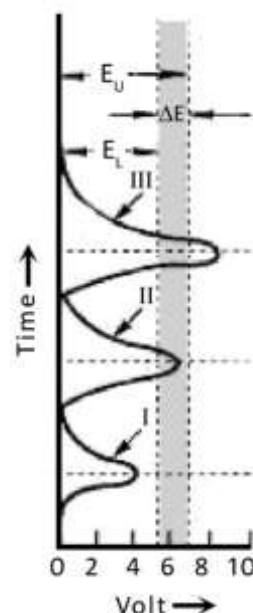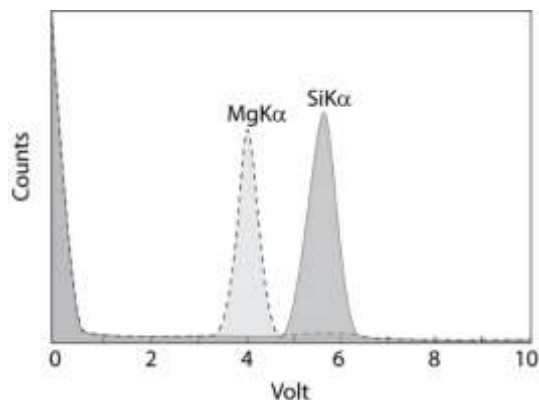
times the energy of MgKα (1.253 keV). Therefore, if the pulse for MgKα is at 4 V, the pulse for SiKα will be at about 4 x 1.4 = 5.6 V.

A typical SCA scan shows noise near 0 V, an escape peak depending on the detector gas and a peak for the x-rays entering the counter. The difference between the voltages of the peak for the incoming x-rays and the escape peak is equal to the difference between the energies of the incoming x-ray and the characteristic x-ray of the detector gas (ArKα or XeLα). An escape peak is produced when x-rays entering the counter have a slightly higher energy (E_{x-ray}) than the critical excitation energy of the detector gas (e.g., $E_{c(K-shell)}$ of Ar) so that the overvoltage is greater than one (e.g., $U = \dfrac{E_{x-ray}}{E_{c(Ar\ K-shell)}} > 1$). Consequently, and the incoming x-rays ionize the atomic inner shells of the detector gas, which fluoresce to produce its characteristic x-rays (e.g. ArKα). The fluoresced x-rays escape from the counter and, as a result, the energy of the incoming x-rays is diminished by an amount equal to the energy of the fluoresced x-rays.
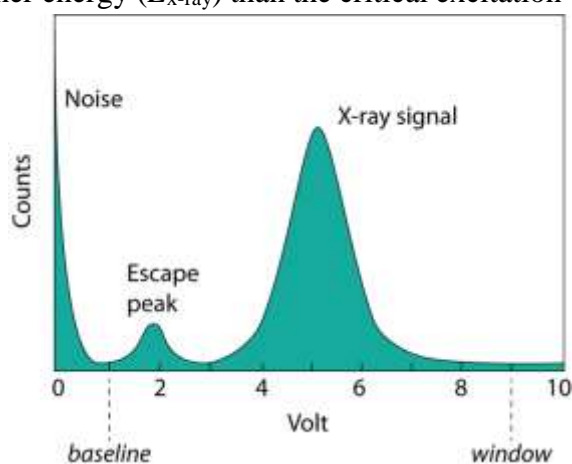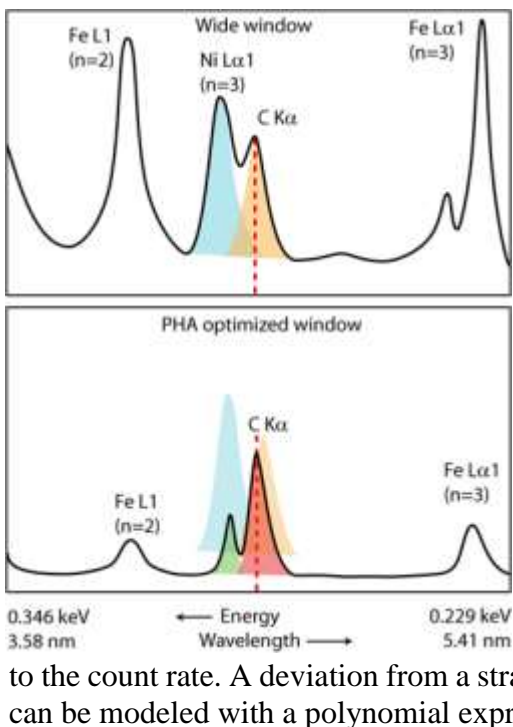

PHA is used to eliminate low energy noise as well as x-ray energies of interfering elements. Higher order ($n>1$) x-rays of transition metals can be efficiently eliminated by optimizing the PHA settings during light element analysis.

The resolution of a proportional counter is the energy width of a peak at FWHM divided by the mean peak energy. A properly functioning counter has Gaussian distribution of pulses and a resolution of between 15 and 20%.

A finite time elapses during which an x-ray pulse processes by the detector system. During this time interval, known as the dead-time, the detector is unavailable to process subsequent pulses. The dead-time corrected count rate is given by $N'/(1-\tau N')$, where N' is the measured count rate, and τ is the dead time. One method of determining τ consists of plotting N' versus the beam current. The beam current is proportional

to the count rate. A deviation from a straight line on the plot is due to the dead-time, which can be modeled with a polynomial expression.

6. COMPOSITIONAL IMAGING BY WDS

The output from the proportional counter of a WD spectrometer can be used to construct an x-ray image (map) showing the spatial distribution of an element in the sample. Elemental x-ray maps are acquired either by beam-rastering in which the electron beam rasters over the area to be imaged, or by stage-rastering in which the electron beam is stationary while the stage moves. A set of elemental maps can be used to identify phases and estimate their proportions in the sample.

The resolution of an x-ray map depends on the step-size for measurements as the beam moves relative to the sample. Each point measurement corresponds to a pixel on the image. The x-ray count rate may be manipulated by changing the beam current, and the total accumulated counts per point can be controlled by changing the dwell-time, i.e., the counting time for each measurement. The quality of an x-ray map depends on the concentration of the element being mapped and differences in its concentration between the different phases in the sample. The acquisition time of x-ray maps mostly depends on the resolution and the dwell time, but it is also limited by the hardware (e.g., stage speed). Mapping a 30 mm x 15 mm area at a resolution of 20 μm and a dwell time of 30 msec requires about 9½ hours.

Elemental maps may provide a complete quantitative analysis at every pixel scanned if the pixel data are corrected for background, divided by standard intensities and corrected for matrix effects. By using several WD spectrometers, the major elements can be mapped simultaneously for matrix corrections. However, because of short dwell-times the chemical composition of each point will be relatively imprecise. Using long dwell-times may result in unacceptably long acquisition times.

6.1. BACKGROUND CORRECTION IN WDS COMPOSITIONAL IMAGING

X-ray maps not corrected for background contain a continuum artifact. Continuum x-ray intensities generated by phases with different mean atomic numbers may be different, and a spurious elemental map may result even if the element is absent in the sample. The following example shows spectra of two phases, a Zn-rich and a Sn-rich phase, present in the sample being mapped. The sample does not contain S. But a map obtained with the spectrometer set to measure S is similar to the Sn map. This is not because the Sn-rich phase contains S. The S map is an expression of the higher background counts measured when the beam interacts with the Sn-rich phase.

Zn x-ray image   Sn x-ray image   S x-ray image
(false background)
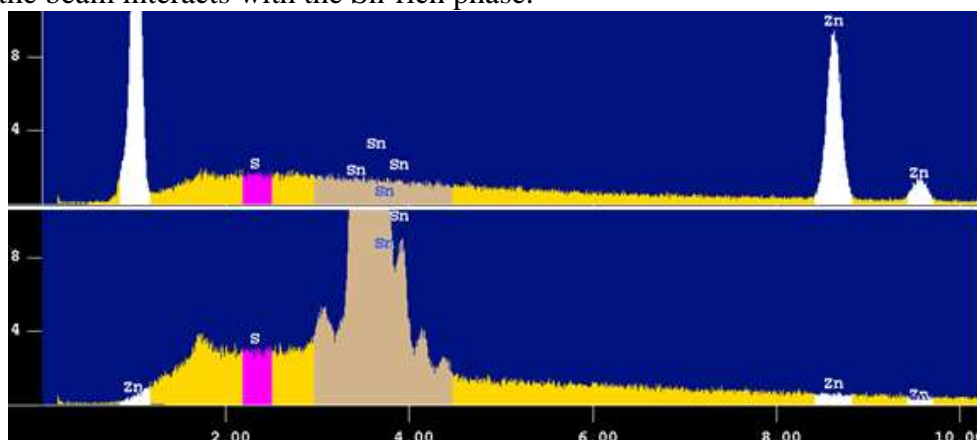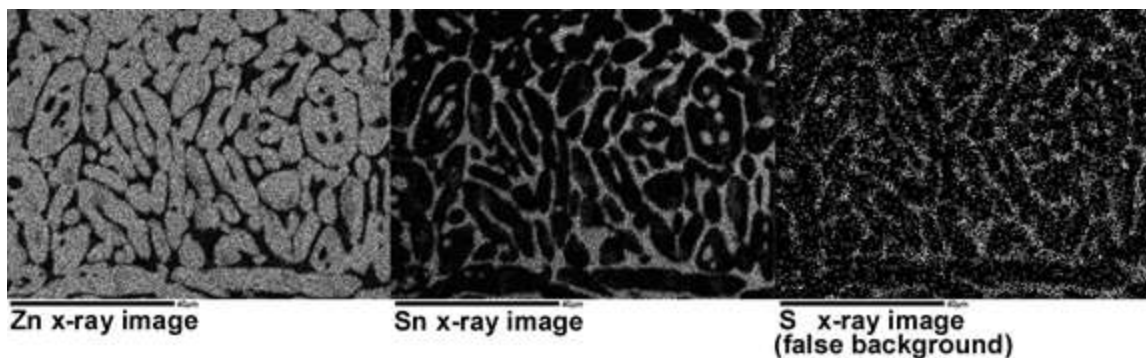
The background map may be actually useful to correct for the background signal in the Sn and Zn maps. However, the background component in the two maps may be different because of variation in the spectrometer response at different x-ray energy ranges, and if the two elements were mapped with different spectrometers. In such a case, separate background maps be required to correct for the background in the Sn and the Zn maps.

6.2. DEFOCUSING IN BEAM-RASTERED WDS X-RAY MAPS

In beam-rastered x-ray mapping, the electron beam may move outside the WDS x-ray focusing ellipsoid that will result in an x-ray signal loss. The counter will intercept more x-rays when they are generated within the focusing ellipsoid, and the map will show higher intensities along the long axis of the ellipsoid. Defocusing is greater at low magnifications because the beam rasters over larger areas.

WDS defocusing during mapping
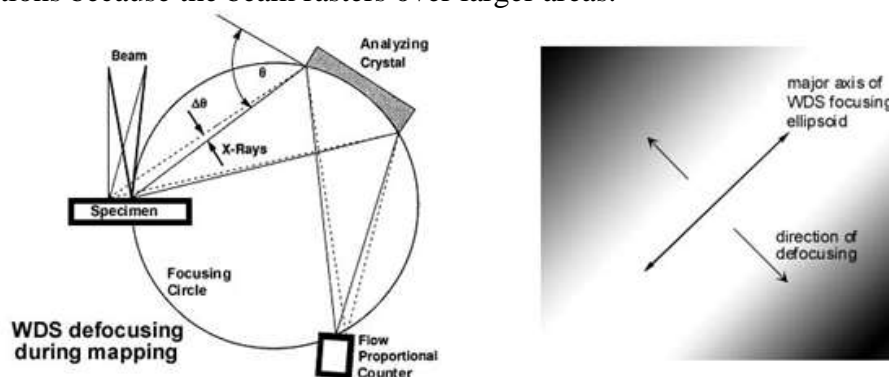
As the beam moves off the optic axis, the displacement in the specimen plane is equivalent to a change in the angle of incidence of the x-rays on the crystal by an angle $\Delta\theta$.

Example of a defocused image

There are four approaches to correct for WDS x-ray defocusing (Newbury et al., 1990):

- *Stage scanning*: Defocusing does not occur in stage-rastered maps because the beam is stationary and vertical during image acquisition.
- *Crystal rocking*: The spectrometer crystal is rocked synchronously with the beam scan to maintain x-ray focus, i.e., the beam is always incident on the center of the x-ray focusing ellipsoid, which changes position as the beam moves.
- *Standard mapping*: The specimen and the standard are mapped under the same condition so that defocusing is identical in both maps. When a k-ratio map is calculated, the defocusing effects cancel out.
- *Peak modeling*: A mathematical expression is used to correct for the intensity loss in the image.

7. QUANTITATIVE ANALYSIS WITH WDS

Quantitative analysis with WDS involves careful sample preparation, setting up the EPMA for analysis, qualitative identification of elements, standard intensity measurements (calibration), measurement of intensities in the specimen, and data reduction by applying matrix corrections to the raw measurements.

7.1. SAMPLE PREPARATION

For qualitative analysis only, the sample may be mounted with double-stick conductive carbon tape on the sample holder. For precise WDS analysis, however, careful sample preparation is essential.

The sample is cut and mounted in epoxy resin, polished first with 240-600 SiC paper (53-16 μm grain size) and then with alumina slurry or diamond paste on cloth (grit size 1.00-0.25 μm). It is washed with water in ultrasonic cleaner after each polishing step, and dried and wiped with ethanol after the final step. For water-soluble materials, the sample is dry polished with fine polishing paper air-dried with a blow duster.
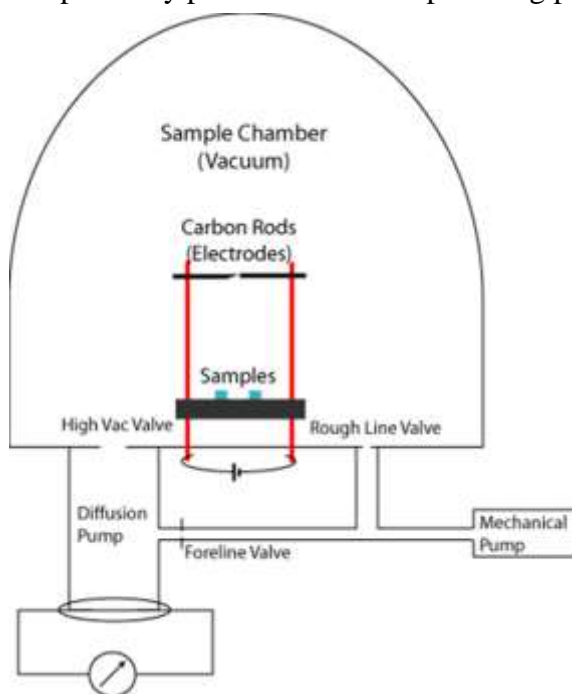
Electrically insulating samples are carbon-coated to ensure current flow from the sample to the ground. The standards and the sample should be coated to the same thickness. Carbon coating is carried out by carbon evaporation under vacuum. A polished brass block is used to monitor the carbon coat thickness. With increasing coat thickness, brass changes color from orange (150 Å) to purple (200 Å), deep blue (250 Å) and metallic blue (> 300 Å). A thickness of about 250 Å is recommended for microprobe analysis at 15-20 kV accelerating voltage.

7.2. SETTING UP THE ELECTRON MICROPROBE

7.2.1. Accelerating voltage

The accelerating voltage depends on overvoltage requirement. E.g., FeKα is not emitted with a 5 keV beam because $E_{c(Fe\ K\text{-shell})} = 7.111$ keV, and $U < 1$. It is worth noting that for a particular accelerating voltage, overvoltage will be different for different elements. U should typically be about 2-10.

7.2.2. Filament saturation and beam alignment

This step involves saturating the filament, setting the gun bias, beam shift and tilt alignment, and wobble and astigmatism correction. Filament current is adjusted to ensure saturation, and gun bias is properly set to ensure optimum emission. The beam current is maximized through shift and tilt alignment. Wobble and astigmatism correction are done with the image. Image defocusing should be symmetrical above and below the optimum beam focusing plane, i.e., the image does not wobble. If there is wobble, the position of the objective lens aperture is fine-adjusted. If the beam spot is elliptical on the image plane, the image is distorted. The stigmator controls are used to obtain a round spot and remove distortion.

7.2.3. Spectrometer choice

E.g., FeKα ($\lambda_{K\alpha}$ = 0.1937 nm, $E_{FeK\alpha}$ = 6.4 keV) can be diffracted by TAP (2d = 2.5757 nm), PET (2d = 0.8742 nm), and LIF (2d = 0.4027 nm). Which crystal is appropriate? For n = 1, equation $\lambda = 2d\sin\theta$, i.e., $\theta = \sin^{-1}\left(\frac{\lambda}{2d}\right)$, and for R = 140 mm, equation $L = n\lambda\frac{140}{d}$ indicate:

> θ = 4.3° and L = 191.2 mm for TAP
> θ = 12.8° and L = 62.0 mm for PET
> θ = 28.8° and L = 134.6 mm for LIF

For good diffraction, θ should be 15-65°, and L-value should be in the mid-range of spectrometer movement (the range for a 140 mm focusing circle is ~60-250 mm). Therefore, LIF is the appropriate choice.

Xe has a better quantum efficiency for FeKα than Ar. So, a Xe counter that comes with a Be window should be selected.

PHA must be performed to set the baseline and window voltages in the SCA. For a Xe counter, the CuKα ($E_{CuK\alpha}$ = 8.04 keV) pulse should be at 5 V with the appropriate voltage in the collection wire. Since $E_{FeK\alpha}$ = 0.8 x $E_{CuK\alpha}$, the FeKα pulse should be at 0.8 x 5 = 4 V.

For higher energy x-rays like FeKα, smaller detector slits are recommended. The 300-550 μm slit should be selected.

7.2.4. Beam current and counting time

These settings depend on the concentration of the element being measured. A higher beam current increases the count rate, and a longer counting time increases the total counts. This *improves the precision and decreases the random error*. Counting statistics dictates that for N counts, the uncertainty is $\pm\sqrt{N}$, or $\frac{\sqrt{N}}{N}$x100%, i.e., $\frac{1}{\sqrt{N}}$x100%. E.g.,

> For 25 counts, the uncertainty is 20 %
> For 100 counts, the uncertainty is 10 %
> For 10,000 counts, the uncertainty is 1 %

7.2.5. Probe diameter

For certain types of analyses, it is necessary to use a defocused beam (large spot size). E.g., if the average composition of a fine-grained material is desired, the spot size should be greater than the grain size. In glass, Na migrates away and F migrates toward the spot. Hydrous samples, salts and some carbonates are susceptible to beam damage. In these cases, a large spot size (~ 10 μm) is used to reduce element migration and beam damage.

7.3. QUALITATIVE ANALYSIS

Quantitative analysis with WDS requires prior knowledge of the presence of elements that are to be measured. Contrast in a backscattered electron image provides some indications of the major compositional differences among the phases. The EDS provides a quick qualitative spectrum. Thus, the combination of a BSE image and EDS spectra is an important tool for quick qualitative analysis.

Phases appearing bright in backscattered-electron image contain heavier elements
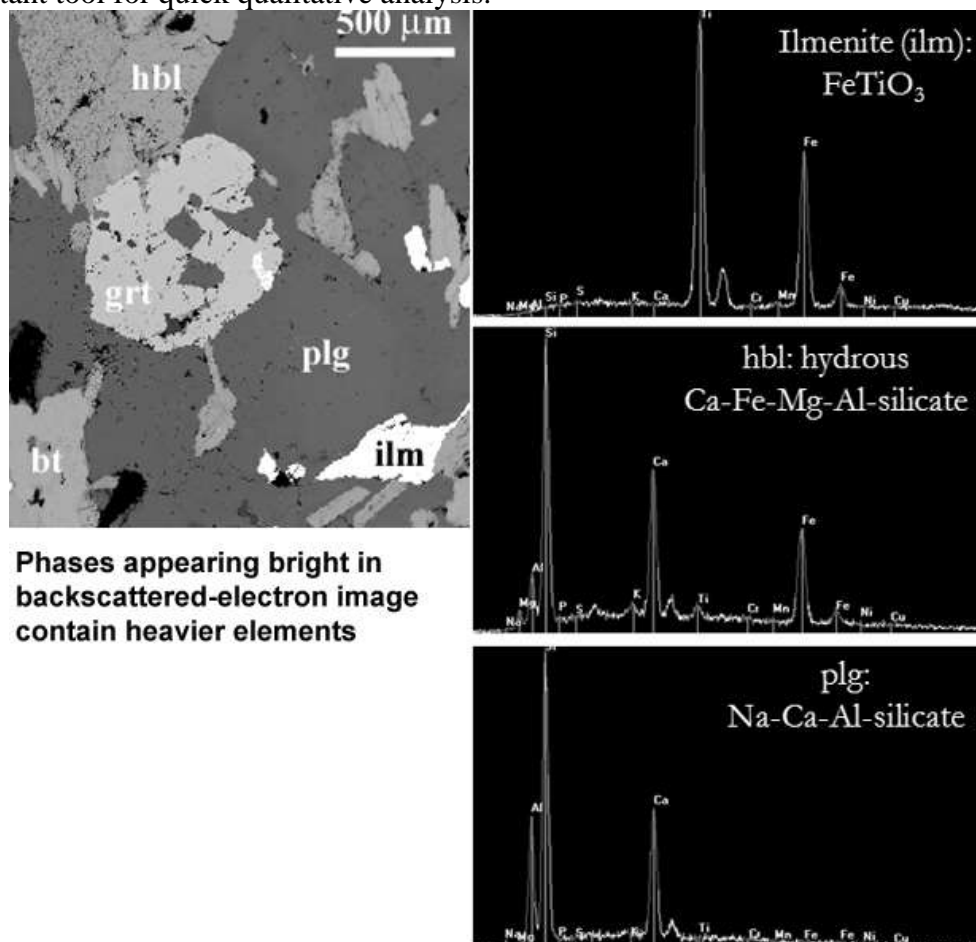
The spectra, however, may fail to register trace elements and may contain peak overlaps. In addition, depending on the window material, the EDS detects elements only above a certain atomic number. With a Be window, only elements above atomic number 9 (F) are detected. Wavelength scans with WDS (qualitative analysis) over a small range of

wavelength may be used to qualitatively identify F, O, N, C and B using layered diffractors (e.g., LDE1 or LDEC). WDS scans may also be used to detect trace elements.

7.4. CALIBRATION AND UNKNOWN ANALYSIS

The analytical conditions (e.g., accelerating voltage, beam current, etc.) are set in the beginning and maintained throughout the session. Standard x-ray intensities of the elements to be measured are obtained on appropriately chosen standards. Different standards may be used for different elements. Secondary standards may be analyzed to check if their known compositions are reproduced. Calibration is important because it *improves the accuracy and decreases the systematic error* (fixed but unknown offset of all measurements from the actual value).

## 7.4.1. Background and Peak Overlap Correction in WDS
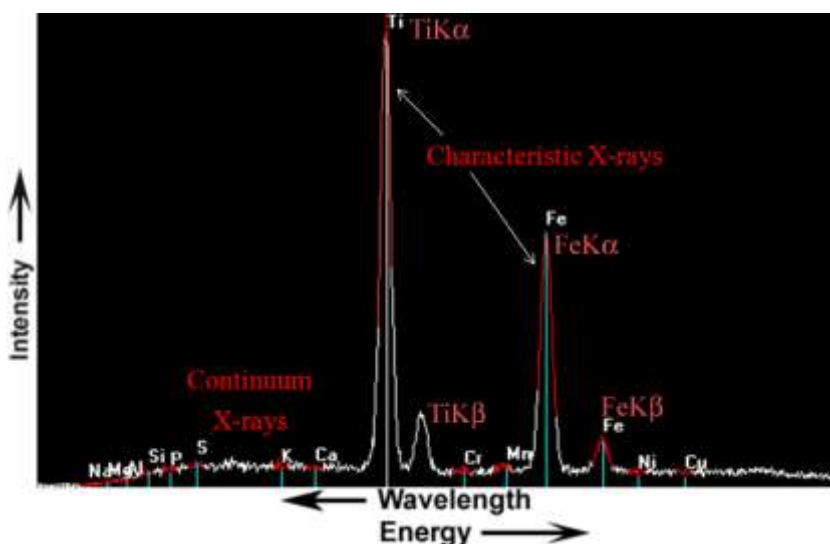
A typical x-ray spectrum consists of characteristic x-ray peaks and a background comprised of continuum x-rays. X-ray spectrometry involves measurement of "peak minus background" or net intensities, i.e., peak intensities corrected for background. The usual method to obtain background intensities is by interpolation. The spectrometer is set to measure count rates on two positions, one on each side of the peak, and the background under the peak is calculated by interpolating between the two measurements.

Peaks recorded in an x-ray spectrum are a convolution of the peak from the characteristic x-rays and the instrumental response. In EDS, the peaks are usually broad due to a large instrumental effect. Because of good spectral resolution in WDS, the tall and
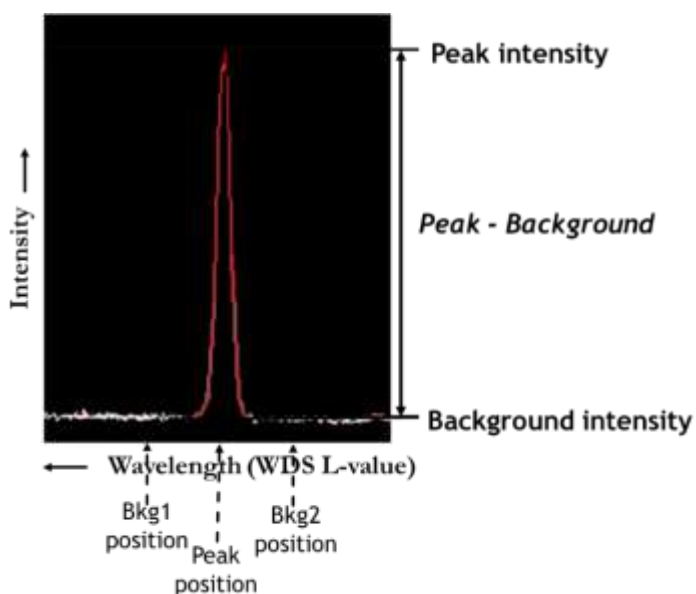
narrow shape of the peaks are retained. However, layered diffractors in WDS yield broad peaks.
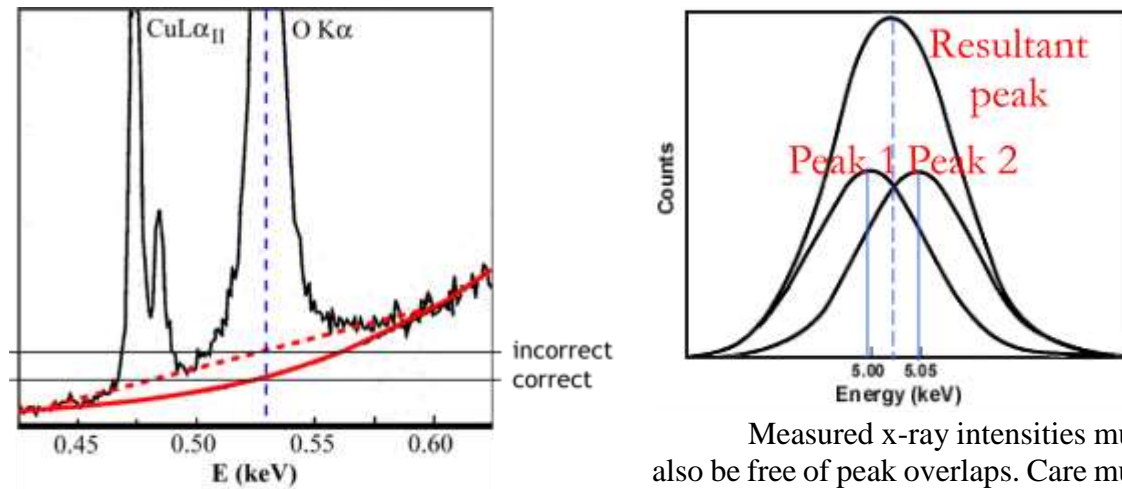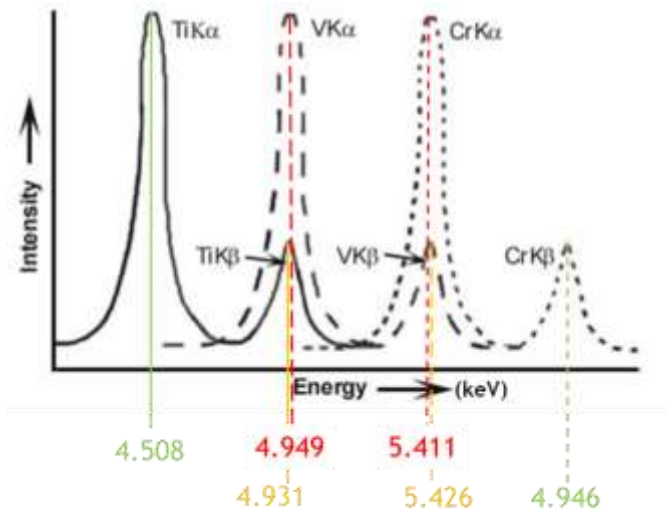

Measured x-ray intensities must also be free of peak overlaps. Care must be taken to avoid interfering peaks of other elements both on the peak and the background positions. When a peak is broad, an overlap between adjacent peaks is possible. Even for partial overlaps, the tails of two adjacent peak may overlap. When broad overlapping peaks are present in the spectrum, background modeling using a polynomial fit may be more appropriate.

In case of unavoidable peak overlaps, the magnitude of an overlap can be calculated by measuring the intensity of the overlapping peak on a standard that contains the interfering element, but not the element of interest. For example, in the Ti-V-Cr system, there are two peak overlaps. The VKα and the CrKα peaks are overalapped by the TiKβ and VKβ peaks, respectively. The intensity contributions from the TiKβ and VKβ peaks must be subtracted from the measured intensities of VKα and CrKα in order to obtain their true intensities. Following is a schematic representation of the x-ray spectrum of a Ti-V-Cr alloy showing the peak overlaps:

The intensities of the VKα and the CrKα may be corrected with to the following equations:

$$I^{corr}_{VK\alpha} = I^{meas}_{VK\alpha} - \frac{I^{meas}_{TiK\alpha}}{I^{Ti\text{-}std}_{TiK\alpha}} I^{Ti\text{-}std}_{VK\alpha}$$

(7.1)

$$I^{corr}_{CrK\alpha} = I^{meas}_{CrK\alpha} - \frac{I^{corr}_{VK\alpha}}{I^{V\text{-}std}_{VK\alpha}} I^{V\text{-}std}_{CrK\alpha}$$

(7.2)

where, I is intensity, "corr" is corrected, "meas" is measured and "std" is standard. To correct the intensity of VKα, $I_{VK\alpha}^{Ti\text{-}std}$ is measured on pure Ti. Since pure Ti does not contain V, the $I_{VK\alpha}^{Ti\text{-}std}$ measured is because of the presence of TiKβ. $I_{VK\alpha}^{Ti\text{-}std}$ is subtracted

from $I_{VK\alpha}^{meas}$ measured in the sample after multiplying it with the k-ratio of TiKα (=$I_{TiK\alpha}^{meas}$ / $I_{TiK\alpha}^{Ti\text{-}std}$) in the sample, which serves as a scaling factor. The correction for CrKα is similar, except $I_{VK\alpha}^{corr}$ is used in Eqn. 6.2 instead of $I_{VK\alpha}^{meas}$.
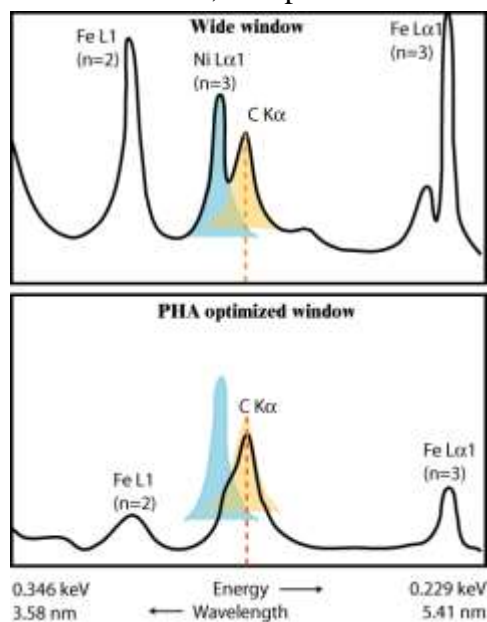
The transition metals Ti, V, Cr, Mn, Fe, Co and Ni, and the metals Zr, Nb and Mo emit x-rays at wavelengths similar to the characteristic wavelengths of the light elements such as F, O, N, C and B. The elements Zr, Nb and Mo also have absorption edges, which greatly diminish the emitted intensities of the light elements. For example, the NKα (31.6 Å) is severely overlapped by TiL1 (31.4 Å). It is thus extremely difficult to measure N in the presence of Ti, especially if N is present in trace amounts. Correctly setting the PHA baseline and window may filter out the higher order x-ray wavelengths. This is demonstrated in the following wavelength scans, in which the higher order lines of Fe and Ni are efficiently subdued and the background lowered with optimal PHA settings for carbon Kα.

8. REFERENCES

Anderson, C.A. and Hasler, M.F. (1966) In *Proc. 4th Intl. Conf. On X-ray Optics and Microanalysis* (R. Castaing, P. Deschamps and J. Philibert, eds.) Hermann: Paris, p. 310.

Bambynek, W., Crasemann, B., Fink, R.W., Freund, H.U., Mark, H., Swift, S.D., Price, R.E. and Rao, P.V. (1972) Rev. Mod. Phys., 44, 716.

Bearden, J.A. (1964) "X-ray Wavelengths", Report NYO 10586, U.S. Atomic Energy Commission, Oak Ridge, Tennessee.

Bence, A.E. and Albee, A. (1968) J. Geol., 76, 382.

Berger, M.J. and Seltzer, S.M. (1964) Nat. Acad. Sci./Nat. Res. Council Publ. 1133, Washington, 205.

Bethe, H. (1933) In *Handbook of Physics*. Springer: Berlin, 24, 273.

Castaing, R. (1951) Ph.D. Thesis, University of Paris.

Duncumb, P. and Reed, S.J.B. (1968) In *Quantitative Electron Probe Microanalysis* (K.F.J. Heinrich, ed.), Nat. Bureau Stand. Spl. Publ. 298, 133.

Duncumb, P. and Shields, P.K. (1966) In *The Electron Microprobe* (T.D. McKinley, K.F.J. Heinrich and D.B. Wittry, eds.), Wiley: New York, p. 284.

Heinrich, K.F.J. (1969) National Bureau of Standards, Technical Note 521.

Heinrich, K.F.J. (1986) In *Proc. 11th Intl. Conf. on X-ray Optics and Microanalysis* (J.D. Brown and R.H. Packwood, eds.), Univ. Western Ontario, London, Ont. Canada, p. 67.

Kanaya, K. and Okayama, S. (1972) J. Phys. D.: Appl. Phys., 5, 43.

Myklebust, R.L., Fiori, C.E. and Heinrich, K.F.J. (1979) Nat. Bureau Stand. Tech. Note 1106.

Newbury, D.E., Fiori, C.E., Marinenko, R.B., Myklebust, R.L., Swyt, C.R. and Bright, D.S. (1990) Anal. Chem., 62, 1159A and 1245A.

Packwood, R.H. and Brown, J.D. (1981) X-ray Spectrom., 10, 138.

Philibert, J. (1963) In *Proc. 34th Intl. Symp. X-ray Optics and X-ray Microanalysis, Stanford University* (H.H. Pattee, V.E. Cosslett and A. Engstrom, eds.) Academic Press: New York, p. 379.

Pouchou, J.L. and Pichoir, F. (1984) Rech. Aerosp., 3, 13.

Reed, S.J.B. (1965) Br. J. Appl. Phys., 16, 913.

Shimizu, R., Kataoka, Y., Ikuta, T., Koshikawa, T. and Hashimoto, H. (1976) J. Phys. D.: Appl. Phys., 9, 101.

Thomas, P.M. (1964) U.K. Atomic Energy Auth. Rept. AERE-R 4593.

Yakowitz, H., Myklebust, R.L. and Heinrich, K.F.J. (1973) Nat. Bureau Stand. Tech. Note 796.

8.1 SOURCES AND ACKNOWLEDGEMENTS

1) Goldstein, J.I., Newbury, D.E., Joy, D.C., Lyman, C.E., Echlin, P., Lifshin, E., Sawyer, L. and Michael, J.R. (2003) *Scanning Electron Microscopy and X-ray Microanalysis* (Third Edition). Kluwer Academic/Plenum Publishers: New York.

2) JEOL technical manuals.